Robust sizing optimization of stiffened panels subject to geometric imperfections using fully nonlinear postbuckling analyses

Kai Steltner[1*], **Benedikt Kriegesmann**[1#], **Claus B.W. Pedersen**[2]

[1]Hamburg University of Technology, Institute for structural mechanics in lightweight design
Am Schwarzenberg-Campus 4, 21073 Hamburg, Germany
**corresponding author: kai.steltner@tuhh.de*
#benedikt.kriegesmann@tuhh.de

[2]Dassault Systèmes Deutschland GmbH
Glockengießerwall 22, 20095 Hamburg, Germany
claus.pedersen@3ds.com

This work presents a new approach for deterministic and robust thickness sizing optimization of a stiffened panel subject to geometric imperfections. Fully nonlinear pre- and postbuckling analyses determine time-dependent reaction forces using the backward Euler integration method. The global buckling resistance is optimized by maximizing the sum of reaction forces in the pre- and postbuckling regions without the necessity to directly evaluate the buckling point. The robust design optimizations consider geometric imperfections as parametrized random fields using an approach based on Fourier series. The first-order second-moment method (FOSM) determines the mean and the variance of the objective function in each optimization iteration. Monte Carlo simulations validate the FOSM approach for the present optimization formulation. The robust optimized designs show significantly increased buckling loads and robustness compared to the initial design and deterministically optimized designs even for the deterministic use case.

Keywords: Sizing optimization, shell structure, robust design optimization, nonlinear postbuckling analysis, manufacturing uncertainty, Taylor series approach, FOSM

1 Introduction

Since Koiter's pioneering work [1], the buckling load of axially compressed cylindrical shells is known to be dependent on geometric deviations, frequently referred to as (geometric) imperfections, from the ideal shell geometry. This holds for unstiffened cylindrical shells as well as for unstiffened and stiffened curved panels [2]. Since these imperfections are unknown during the design phase, their influence is often accounted for by knockdown factors (e.g. [3]) having turned out to be overly conservative for modern shell manufacturing [4]. Hence, various researchers suggested to use probabilistic methods for the design of shell structures to consider geometric imperfections as random parameters or random fields, respectively (see, e.g. [5]–[7]). The buckling optimum is heavily dependent on the design approach considered [8] when searching for the optimal design of cylindrical shells. Considering a probabilistic design approach in the optimization is equivalent to performing robust design optimization (RDO) or reliability-based design optimization (RBDO), which are broad research fields (see, e.g. [9, 10]).

Stiffened shells tend to be less sensitive to geometric variations. Moreover, the first bifurcation point along the equilibrium paths is typically associated with buckling of the skin between the stiffeners and reduces only slightly the overall buckling resistance [11], and it is not considered the driver for the global buckling designing. Therefore, this so-called skin-buckling is partially allowed in the design of airframe structures. The stiffeners start to buckle at a higher load level accompanied by a significant loss of stiffness, and for certain designs a significant drop of the load carrying capacity, i.e. a snap through point, is present. Hence, the design of curved stiffened panels requires nonlinear analyses far into the postbuckling range. Thereby, the analysis is computationally expensive and numerically challenging, especially for the design optimization of such panels for buckling resistance. This observation is even more pronounced for RDO or RBDO approaches requiring supplementary computational resources compared to a conventional deterministic optimization. Therefore, previous work addressing robust buckling design optimization of stiffened panels applies simplified buckling analyses or surrogate models, considering a very limited set of design variables and/or random variables.

Deterministic optimization of stiffened panels was, for instance, conducted by Lamberti et al. [12], who used a semi-analytical approach for the buckling analyses. Optimization based on finite element models was, for instance, carried out by Fleury et al. [13], who determined buckling loads from eigenvalue analyses but did not consider the robustness with respect to geometric imperfections.

Qu and Haftka [14] performed RBDO of stiffened panels using Monte Carlo simulations of a surrogate model, considering four design variables. Bacarreza et al. [15] employed an evolutionary algorithm to solve a multi-objective optimization, using an artificial neural network as a surrogate model. Meng et al. [16] considered a simplified smeared stiffener model for the buckling analyses, using particle swarm for RBDO. The simplified model was later augmented by employing a surrogate model [17]. López et al. [18] employed a genetic algorithm for RBDO for which the embedded most probable point search is conducted on a surrogate model. Kriegesmann et al. [19] used a genetic algorithm for RBDO of stiffened panels.

Multiple of the aforementioned work considered composite shells that have a very low number of design variables, enabling the use of non-gradient-based optimization approaches. However, nonparametric design optimization approaches such as free sizing, shape or topology optimization consider a much larger number of design variables. The amount of design variables renders the use of the non-gradient-based optimization approaches infeasible [20]. Hence, efficient RDO requires the computation of the gradients of the objective function including the gradients of the probabilistic measures.

A general approach for determining the gradients of the mean and the variance of structural responses was proposed by Doltsinis et al. [21, 22]. Here, the nonlinear equilibrium equations are perturbed with respect to the random parameters. Solving the resulting set of equations allows computing the desired gradients. The computational effort of this method is high, as it scales with the number of random parameters and is highly intrusive with respect to the numerical implementation. A numerically more efficient approach for RDO was presented by Kriegesmann and Lüdeker [23] for the case of topology optimization. Here, the adjoint method is applied for calculating the gradients of the stochastic moments, requiring one additional equation system to be solved per optimization iteration. This approach is even more intrusive with respect to the numerical implementation since the gradients have to be derived and implemented for each combination of structural responses (stress, compliance, …), design variables (shape, topology, …) and random parameters (geometry, material, …). Instead, we suggest an approach where mixed derivatives are determined using gradients by the adjoint method for the design variables and gradient approximations by finite differences for the random variables as explained in the following.

For deterministic optimization, general formulations for determining the gradients of linear and nonlinear problems using the adjoint method are found in [24, 25]. Thereby, the gradients for various combinations of the optimization objectives and the design variables are known and available in commercial software. The current work combines the approach presented in [23] with the adjoint gradients available for deterministic optimization.

The current work presents a new approach for RDO of stiffened panels, applying a numerical implementation for the robust design optimization analogous to [26]. The approach in [26] examines static topology optimization considering stiffness and strength whereas the present work considers sizing buckling optimization of stiffened panels and manufacturing imperfections as random variables.

Furthermore, the present work applies quasi-static modeling using a backward Euler method for the time integration when determining the deformation in the pre- and postbuckling range. The approach incorporates a geometrically nonlinear analysis for the global buckling point and for the postbuckling behavior of stiffened panels. An efficient gradient based optimization algorithm is employed for increasing the buckling resistance. The gradients of the objective function are determined using the adjoint method, and hence the computational cost is independent of the number of design variables. Thereby, the approach can address applications where the number of design variables is equal to the number of elements of the finite element model. Additionally, the efficient first-order second-moment method is employed for robust design optimization. The method uses a semi-analytical approach for the uncertainty quantification of the manufacturing imperfections. Three problem formulations of deterministic sizing optimization are discussed and considered for robust design optimization afterwards.

The paper is organized as follows. Section 2 summarizes the theory and methodology for the present work. The problem formulation for the deterministic sizing optimization is defined prior to the approach for the robust design optimization and the corresponding numerical implementation. The section also defines the parametrization of the geometric imperfections as well as the backward Euler integration solving the structural equilibrium. Section 3 describes the geometry, material properties and the finite element model considered for the present work. The following section 4 discusses the results of the deterministic and the robust sizing optimization. General conclusions and numerical observations with respect to the industrial applications are summarized in section 5.

2 Methodology

Initially, we describe the deterministic optimization formulation for maximizing buckling resistance using thickness sizing optimization. The backward Euler integration scheme and the adjoint sensitivities are discussed. Secondly, we extend the optimization formulation to a robust optimization formulation using a nonintrusive approach for considering manufacturing imperfection uncertainties. Finally, the parametrization of the geometric imperfections for the finite element model is defined.

2.1 Deterministic sizing optimization

The optimization target for the sizing optimization of stiffened panels is to increase the buckling carrying capacity for a given mass. A characteristic deformation curve for a panel structure is presented in Figure 1a, showing the reaction force as a function of a prescribed displacement and a significant buckling point. Maximizing the buckling point $F_{Buckling}$ can be formulated in various ways. Previously, the reaction force characteristic for buckling structures is optimized for obtaining a desired reaction force history for crashworthiness applications, see [27]. Here, we decide as objective to maximize the sum of the reaction forces F_i given at specified discrete prescribed displacement points $u_{p,i}$ as shown in Figure 1a subject to a mass constraint. The mass of the initial design $m_{initial}$ is applied as a mass constraint. Hence, we obtain the following optimization problem for the deterministic optimization:

$$\begin{aligned} \max_{\mathbf{t}} F_{Sum} &= \sum_{i=1}^{I} F_i(u_{p,i}, \mathbf{t}) \\ s.t. \quad m &\le m_{initial} \\ \mathbf{R}(u_i, \mathbf{t}) &= 0 \\ \underline{\mathbf{t}} \le \mathbf{t} &\le \bar{\mathbf{t}} \end{aligned} \tag{1}$$

where $\mathbf{R}$ is the residual of the quasi-static state equation defined in Eq. (2), and $\underline{\mathbf{t}}$, $\bar{\mathbf{t}}$ are the lower and upper bounds of the thickness design variables defined by the vector $\mathbf{t}$. Physical and numerical observations verified that the optimization formulation in Eq. (1) is sound for sizing optimization, implicitly maximizing the buckling point $F_{buckling}$ for stiffened panel applications. The strains both in the pre- and the postbuckling range are modeled using an elastic constitutive material and small strain $\varepsilon(u)$ assumption, as the representative strains for the present applications are well below $\varepsilon = 0.01$. The bending deformation in the prebuckling range in Figure 1a is negligible and only normal stresses are present. Thus, the reaction forces and deformation in the compressive pre-buckling range is approximated by $F = EA\varepsilon(u_p)$ where E is the Young's modulus and A is the representative cross-section area. The mass is constrained to be less-equal to the initial mass in Eq. (1). Numerical studies show that the mass constraint is active for all optimizations. Furthermore, the sum of the representative cross-section areas in the compression direction is almost constant and independent of the thicknesses defined as the design variables. Thereby, the reaction force in the prebuckling range is a constant linear function of the prescribed displacement $F \sim u_p$ and practically independent of the design variables as well. The value of the buckling point $F_{Buckling}$ is determined by the bending moment of inertia. Therefore, the values of the reaction forces for specified prescribed displacement points in the postbuckling range in Figure 1a depend profoundly on the thickness design variables. Consequently, the optimization formulation in Eq. (1) will primarily increase the reaction forces at the buckling point and the reaction forces in the postbuckling range. Thereby, the prescribed displacement point for which the critical buckling appears is also increased. The numerical observations for all the present examples confirm this theoretical deduction. Note, this optimization formulation per default also has the advantage incorporated that it will avoid including any local buckling modes which are not important for the global buckling of the structure and therefore, these local buckling modes are of no practical interest for the optimization when maximizing the global buckling resistance.

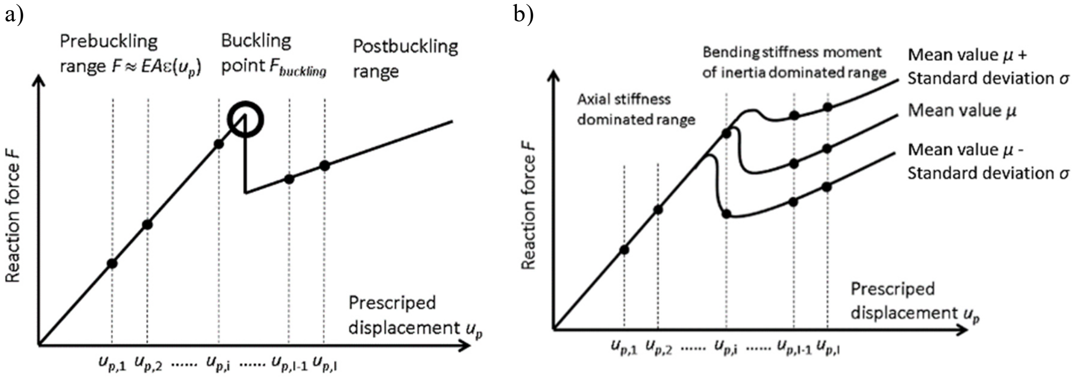

Figure 1: Qualitative plots for (a) reaction force of curved shell structure highlighting buckling point and (b) stochastic variation with respect to geometric manufacturing imperfections.

2.1.1 Quasi-static equilibrium modeling using backward Euler integration

The present work applies quasi-static finite element modeling using backward Euler integration [28, 29] for the equilibrium analysis as implemented in the finite element solver Abaqus [30]:

$$
\begin{aligned}
&\mathbf{R}_n = \mathbf{0} = \mathbf{I}(\mathbf{u}_n, \mathbf{u}_{n-1}, \mathbf{t}) - \mathbf{F}(u_{p,i}, \mathbf{t})_n + \mathbf{M}\ddot{\mathbf{u}}_n \\
&\ddot{u}_n = \frac{u_n - u_{n-1}}{\Delta\xi^2} - \frac{\dot{u}_{n-1}}{\Delta\xi} \qquad (2) \\
&\dot{u}_n = \frac{u_n - u_{n-1}}{\Delta\xi} \quad \text{where} \quad \Delta\xi = \xi_n - \xi_{n-1} \quad \text{for} \quad n = 1, 2, \ldots, N-1, N
\end{aligned}
$$

and the time ξ should be seen as a pseudo-time where the total time is always set to $\xi_N = 1$. The discretized deformations, velocities and acceleration are defined by u, $\dot{u}$ and $\ddot{u}$, respectively. The residual vector **R** of the quasi-static state equation is determined by the vector of internal forces **I**, the reaction forces **F** and inertia forces calculated by the mass matrix **M** and the accelerations $\ddot{\mathbf{u}}$. The S4 element is applied, being a 4-node general-purpose shell-element for large displacement and finite membrane strains [30]. Note that for Eq. (2) we can include nonlinearities in the finite element model, such as large deformations, nonlinear constitutive materials and general contact, being integrated in the finite element solver Abaqus [30]. We only need to consider large displacement modeling for the present work. The finite element system in Eq. (2) is solved using a Newton-Raphson iteration scheme and a direct solver. When the time increment size $\Delta\xi$ decreases for the backward Euler scheme in Eq. (2), the numerical damping increases and adds stabilization when solving for equilibrium at the buckling point and in the postbuckling range, which stabilizes the numerical solving of the quasi-static equilibrium for the buckling. An extensive study of the increment size $\Delta\xi$ was carried out to verify that the numerical damping does not physically change the determined structural response and buckling behavior for the present work by comparing the external work, internal energy and kinetic energy of the structure presented in section 3.

2.1.2 Adjoint discrete quasi-static sensitivities

We apply discrete adjoint sensitivities [24, 25, 30, 31] for deriving the reaction force sensitivities with respect to the thickness design variables, as we have few reaction force responses compared with the number of thickness design variables. It is also important to notice that a *continuous* adjoint sensitivity approach typically fails due to the few time increments for the equilibrium integration [24, 32]. The purpose of the present work is not to give a detailed theoretical review on discrete adjoint sensitivities, and theoretical details can be found in [24, 25, 31, 32]. Instead, an overview of the present applied numerical implementation [30] is shortly outlined. One of the main challenges and barriers for a numerical implementation of transient nonlinear discrete adjoint sensitivities is the efficient calculation and storage of all state variables and operators from the primal solution of the backward Euler integration in Eq. (2). These state variables and operators from the primal solution are stored in a database provided by Abaqus [30]. Subsequently, the global operators of the forward pass for the primal solution are reused for the discrete adjoint backward integration and thereby, the adjoint sensitivities are calculated. The present implemented industrial framework in Abaqus supports both shared (SMP) and distributed (DMP) memory parallelization.

2.2 Nonintrusive robust sizing optimization

The current section describes the optimization setup for robust design optimization in the context of a sizing optimization. The probabilistic approach and the corresponding gradients for mathematical programming optimization are presented.

2.2.1 Robust design optimization approach

The objective function $F_{Sum}(\mathbf{t}, \mathbf{a})$ is considered as a function of the design vector $\mathbf{t}$ and the random vector **A**. The optimization is constrained by a global mass constraint as denoted in Eq. (1). The parametrization of the random field of geometric imperfections using a Fourier series is given in section 2.3. The Fourier coefficients A_{kl} are assembled in the random vector **A**. The sum of transient reaction forces F_{Sum} is randomly distributed due to the variability of **A**. The characteristic stochastic moments are the mean value μ and the standard deviation σ as shown in Figure 1b. The robust design optimization aims at simultaneously minimizing the mean value μ and the standard deviation σ of the sum of reaction forces $F_{Sum} = \sum_{i=1}^{I} F_i(u_{p,i}, \mathbf{t})$. This yields the following optimization problem formulation for the objective function $\tilde{F}_{Sum}$:

$$
\begin{aligned}
&\max_{\mathbf{t}} \widetilde{F}_{Sum} = \mu + \kappa \sigma \\
&\text{s.t.} \quad m \leq m_{initial} \\
&\qquad \mathbf{R}(u_i, \mathbf{t}) = \mathbf{0} \\
&\qquad \underline{\mathbf{t}} \leq \mathbf{t} \leq \bar{\mathbf{t}}
\end{aligned}
\tag{3}
$$

The constant κ is the weight factor for the standard deviation. The present formulation in Eq. (3) is a multi-objective optimization problem where varying κ provides the Pareto front.

The derivative of the probabilistic objective $\tilde{F}_{Sum}$ is determined by

$$
\frac{d\widetilde{F}_{Sum}}{dt_e} = \frac{d\mu}{dt_e} + \kappa \frac{1}{2\sigma} \frac{d\sigma^2}{dt_e} \tag{4}
$$

The probabilistic methods used in the following determine the mean value μ, the variance σ^2 and their gradients.

In general, the mean value and the variance of the function F_{Sum} subject to random variables $\mathbf{Z}$ are defined by

$$
\mu = \int_{-\infty}^{\infty} F_{Sum}(\mathbf{z})\, f_{\mathbf{Z}}(\mathbf{z})\, d\mathbf{z} \qquad \text{and} \qquad \sigma^2 = \int_{-\infty}^{\infty} \left(F_{Sum}(\mathbf{z}) - \mu\right)^2 f_{\mathbf{Z}}(\mathbf{z})\, d\mathbf{z} \tag{5}
$$

where the function $f_{\mathbf{Z}}(\mathbf{z})$ defines the probability density function of the random vector $\mathbf{Z}$. In this work, the vector $\mathbf{Z}$ originates from a transformation of the correlated vector $\mathbf{X}$ to the uncorrelated vector $\mathbf{Z}$, see section 2.3.2.

The Monte Carlo method is the simplest but numerically most expensive approach to determine μ and σ. For that, m realizations $\mathbf{z}^{(i)}$ of $\mathbf{Z}$ are generated based on its distribution, and F_{Sum} is numerically evaluated for each realization. Then the mean and variance using the Monte Carlo method are estimated using

$$
\mu \approx \frac{1}{m} \sum_{i=1}^{m} F_{Sum}\left(\mathbf{z}^{(i)}, \mathbf{t}\right) \qquad \text{and} \qquad \sigma^2 \approx \frac{1}{m-1} \sum_{i=1}^{m} \left[F_{Sum}\left(\mathbf{z}^{(i)}, \mathbf{t}\right) - \mu \right]^2 \tag{6}
$$

The number of realization m must be very large for an accurate estimation. The computational cost of the Monte Carlo simulation scales with the number of realizations m. Especially when each realization is the solution of a full finite element analysis, the Monte Carlo approach is numerically very expensive. The Monte Carlo method is only applied for verification and validation of the optimization results in the present work. The efficiency of the Monte Carlo simulation is increased by reducing the number of realizations considered for the estimation Eq. (6) as importance sampling (see, e.g. [33]), use of surrogate models [34] and multilevel approaches [35], respectively. However, all the present Monte Carlo simulation approaches are considered computationally too expensive for the present non-parametric optimization including uncertainties.

Consequently, a different approach is applied for estimating the stochastic moments. The approach is based on a Taylor series expansion of the function F_{Sum} at the mean vector $\boldsymbol{\mu}_{\mathbf{Z}}$ of the random input vector $\mathbf{Z}$. The approach is referred to as first-order second-moment (FOSM) method [23] or method of moments [36]. It is similar to the perturbation approach used by [21, 37]. The Taylor expansion of F_{Sum} at $\boldsymbol{\mu}_{\mathbf{Z}}$ reads

$$
F_{Sum}(\mathbf{z}) = F_{Sum}(\boldsymbol{\mu}_{\mathbf{Z}}) + \sum_{i=1}^{n} \frac{\partial F_{Sum}(\boldsymbol{\mu}_{\mathbf{Z}})}{\partial z_i} (z_i - \mu_i) + \frac{1}{2} \sum_{i=1}^{n} \sum_{j=1}^{n} \frac{\partial^2 F_{Sum}(\boldsymbol{\mu}_{\mathbf{Z}})}{\partial z_i \, \partial z_j} (z_i - \mu_i)(z_j - \mu_j) + \ldots \tag{7}
$$

where n is the number of entries z_i of $\mathbf{Z}$ (i.e. the number of random parameters) and μ_i are the entries of $\boldsymbol{\mu}_\mathbf{Z}$. Inserting Eq. (7) into Eq. (5) and utilizing that the entries of $\mathbf{Z}$ are uncorrelated yields

$$\mu = \int_{-\infty}^{\infty} F_{Sum}\left(\mathbf{z}\right) f_\mathbf{Z}\left(\mathbf{z}\right) d\mathbf{z} = F_{Sum}\left(\boldsymbol{\mu}_\mathbf{Z}\right) + \frac{1}{2}\sum_{i=1}^{n} \frac{\partial^2 F_{Sum}\left(\boldsymbol{\mu}_\mathbf{Z}\right)}{\partial z_i} \sigma_{z,i}^2 + \ldots \tag{8}$$

and

$$\sigma^2 = \int_{-\infty}^{\infty} \left(F_{Sum}\left(\mathbf{z}\right) - \mu\right)^2 f_\mathbf{Z}\left(\mathbf{z}\right) d\mathbf{z} = \sum_{i=1}^{n} \frac{\partial F_{Sum}\left(\boldsymbol{\mu}_\mathbf{Z}\right)}{\partial z_i} \sigma_{z,i}^2 + \ldots \tag{9}$$

Considering only linear terms is referred to as first-order second-moment method for Eqs. (8) and (9). The FOSM approximation of the stochastic moments for the specific use case is validated using Monte Carlo simulations.

2.2.2 Nonintrusive determination of gradients

The derivatives with respect to the design variables $\partial F_{Sum}/\partial t_e$ are determined using the adjoint sensitivity approach as outlined in section 2.1.2. When using the Monte Carlo method, the gradients of the mean value and the variance are implemented as

$$\frac{d\mu}{dt_e} \approx \frac{1}{m}\sum_{i=1}^{m} \frac{\partial F_{Sum}\left(\mathbf{z}^{(i)}, \mathbf{t}\right)}{\partial t_e} \quad \text{and} \quad \frac{d\sigma^2}{dt_e} \approx \frac{2}{m-1}\sum_{i=1}^{m} \left[F_{Sum}\left(\mathbf{z}^{(i)}, \mathbf{t}\right) - \mu\right] \frac{\partial F_{Sum}\left(\mathbf{z}^{(i)}, \mathbf{t}\right)}{\partial t_e} \tag{10}$$

The value $F_{Sum}(\mathbf{z}^{(i)}, \boldsymbol{t})$ and the gradient $\partial F_{Sum}/\partial t_e$ are obtained from the same solutions of the residual $\mathbf{R}$ evaluated for Eq. (6).

The derivative of the mean value using the FOSM approach is given by

$$\frac{d\mu}{dt_e} = \frac{\partial F_{Sum}\left(\boldsymbol{\mu}_\mathbf{Z}, \mathbf{t}\right)}{\partial t_e} \tag{11}$$

and the derivative of the variance is given by

$$\frac{d\sigma^2}{dt_e} = 2\sum_{i=1}^{n} \frac{\partial^2 F_{Sum}\left(\boldsymbol{\mu}_\mathbf{Z}, \mathbf{t}\right)}{\partial z_i \partial t_e} \frac{\partial F_{Sum}\left(\boldsymbol{\mu}_\mathbf{Z}, \mathbf{t}\right)}{\partial z_i} \sigma_{z,i}^2 \tag{12}$$

The computation of the variance Eq. (9) and its derivative Eq. (12) requires the derivatives of F_{Sum} with respect to the random parameters z_i and the mixed derivatives $\partial^2 F_{Sum}/\partial z_i \partial t_e$. Kriegesmann [23] determined the mixed derivatives analytically using the adjoint method for a topology optimization minimizing the mean and variance of the compliance subject to a random Young's modulus or random geometrical properties. The implementation requires only one adjoint system to be solved in addition to the structural residual $\mathbf{R}$ for the equilibrium. However, the numerical implementation in [23] is highly intrusive, as it requires the analytical implementation of the sensitivities for each combination of objective function and constraints, design variable types (e.g., relative densities, nodal coordinates, thicknesses, …) and random parameter types (e.g., Young's modulus, load direction, geometry …).

In consequence, we propose using nonintrusive finite differences with the step size Δz_i for approximating the gradients with respect to random parameters as

$$\frac{\partial F_{Sum}\left(\boldsymbol{\mu}_\mathbf{Z}, \mathbf{t}\right)}{\partial z_i} \approx \frac{F_{Sum}\left(\mu_1, \ldots, \mu_i + \Delta z_i, \ldots, \mu_n, \mathbf{t}\right) - F_{Sum}\left(\boldsymbol{\mu}_\mathbf{Z}, \mathbf{t}\right)}{\Delta z_i} \tag{13}$$

$$\frac{\partial^2 F_{Sum}\left(\boldsymbol{\mu}_{\mathbf{Z}},\mathbf{t}\right)}{\partial z_i \partial t_e} \approx \frac{\dfrac{\partial F_{Sum}\left(\mu_1,\ldots,\mu_i+\Delta z_i,\ldots,\mu_n,\mathbf{t}\right)}{\partial t_e} - \dfrac{\partial F_{Sum}\left(\boldsymbol{\mu}_{\mathbf{Z}},\mathbf{t}\right)}{\partial t_e}}{\Delta z_i} \tag{14}$$

Equations (13) and (14) are determined using the same simulation, i.e. $n + 1$ simulations have to be carried out in total, where n equals the number of random parameters (i.e. the length of $\mathbf{Z}$). $2n + 1$ simulations have to be computed if central differences are applied for Eqs. (13) and (14). Note that the derivatives $\partial F_{Sum}/\partial t_e$ with respect to the design variables t_e are determined from the same simulations using the adjoint sensitivity approach. Therefore, robust design optimization using FOSM and the present finite difference approach in Eqs. (13) and (14) is computationally favorable compared to the numerically costly Monte Carlo method when the number of random parameters z_i is small (e.g., $n \leq 50$).

The linearization of the gradients in Eqs. (13) and (14) with respect to design variables t_e and the random parameters z_i are only quantitatively valid in a given interval of t_e and z_i. However, numerical experiments show that the gradient approximation in Eqs. (13) and (14) can still qualitatively capture the overall behavior of the function F_{Sum} optimized in Eq. (3) when used for a larger interval of z_i [7].

2.3 Parametrization of manufacturing imperfections

Geometric imperfections $\overline{w}(x,y)$ of a curved panel are considered as a two-dimensional random field where x is the axial direction of the panel, y describes the circumferential axis and $\overline{w}$ points inward to the center of the panel curvature. The field is parameterized using Fourier series approximations. The Fourier coefficients are transformed and reduced to a set of uncorrelated parameters. Both applied methods are described in the following section.

2.3.1 Fourier-Series

Geometric imperfections of (mostly cylindrical) shells are traditionally often described in terms of Fourier series (see, e.g., [38, 39]). In difference to cylindrical shells, the imperfection pattern $\overline{w}$ of a panel is not a periodic function. Therefore, the best approximation is provided by the half-wave cosine approach given by

$$\overline{w}(x,y) = 4t_{initial}\sum_{k=0}^{n_x}\sum_{l=0}^{n_y} A_{kl}\cos\frac{k\pi x}{L}\cos\frac{l\pi y}{L_a} \tag{15}$$

Here, L and L_a are axial length and the width of the panel. The Fourier coefficient A_{kl} is the amplitude of an imperfection mode with k axial and l circumferential half waves. The thickness $t_{initial}$ is considered only for normalizing the Fourier coefficients.

The imperfection data used in this study are published in [11] and decomposed into Fourier series for the work in [40]. These panels are constructed of composite materials where the present work considers constitutive isotropic material modeling. However, it is still assumed that these imperfections are representative for industrial metallic panels and plates.

2.3.2 Reduction of parameters

The parametrization of manufacturing imperfections described in the previous section uses a large amount of Fourier coefficients for accurate representation. A reduction of parameters is performed to increase the computational efficiency when considering the imperfections for robust design optimization. A variant of Mahalanobis transformation [41], similar to principal component analysis, is applied for parameter reduction. The transformation relates the random vector $\mathbf{A}$ to the random vector $\mathbf{Z}$ as follows:

$$\mathbf{A} = \mathbf{\Sigma}^{\frac{1}{2}}\mathbf{z} + \boldsymbol{\mu} \quad \text{and} \quad \mathbf{z} = \mathbf{\Sigma}^{\frac{1}{2}}(\mathbf{A} - \boldsymbol{\mu}) \tag{16}$$

The random vector **A** contains n Fourier coefficients A_{kl}, and **Z** is a random vector of uncorrelated zero-mean random parameters having a standard deviation of one. The mean vector $\boldsymbol{\mu}$ and the covariance matrix $\mathbf{\Sigma}$ are determined from m measurements. If the number of measurements m is smaller than the number of random parameters n, the covariance matrix is singular and has many eigenvalues equal to zero. Then, the root of $\mathbf{\Sigma}$ is determined by spectral decomposition and yields the matrix $\mathbf{B} \in \mathbb{R}^{n\times r}$ as

$$\mathbf{\Sigma}^{\frac{1}{2}} = \mathbf{B} = \mathbf{Q}\,\mathbf{D}^{\frac{1}{2}} = (q_1,\dots,q_r)\,diag(\sigma_1,\dots,\sigma_r) \tag{17}$$

The eigenvectors of $\mathbf{\Sigma}$ form the matrix **Q** and the eigenvalues σ_i^2 are the diagonal elements of the matrix **D**. Then, the matrix **B** is used for the Mahalanobis transformation (16) yielding the random vector **z** of length $r < m$, where r is the rank of the covariance matrix $\mathbf{\Sigma}$, as given by

$$\mathbf{A} = \mathbf{B}\,\mathbf{z} + \boldsymbol{\mu} \quad \text{and} \quad \mathbf{z} = \mathbf{B}^{-1}(\mathbf{A} - \boldsymbol{\mu}) \tag{18}$$

When choosing n_x and n_y equal to 20, **A** has the length $n = 21 \cdot 21 = 441$. The length of **Z** equals $r = 7$ when $m = 8$ sets of measurement data are available.

2.4 Numerical implementation

Figure 2 shows the numerical implementation of the robust design optimization. The workflow is implemented using Abaqus [30], Tosca [42], Isight [43] and additional scripting in Python. Tosca provides the optimization framework for defining the thickness design variables, the optimization objective and constraints. Isight and additional Python scripts are applied for calculating the mixed derivatives with respect to the random parameters and the thickness design variables using finite difference calculations. The finite difference calculations are implemented using parallel execution in Isight on an high performance computing (HPC) cluster to reduce the overall runtime. The nonlinear buckling analyses are solved using the backward Euler integration presented in section 2.1.1 using Abaqus. The adjoint derivatives with respect to the thickness design variables for the optimization are also implemented in Abaqus. A python script computes the objective for the robust sizing optimization. The design variables are updated in each optimization iteration using mathematical programming based upon the Method of Moving Asymptotes (MMA) approach as implemented in Tosca. The optimization is considered as converged when the relative change of the objective or the thickness design variables is less or equal to 0.1%.

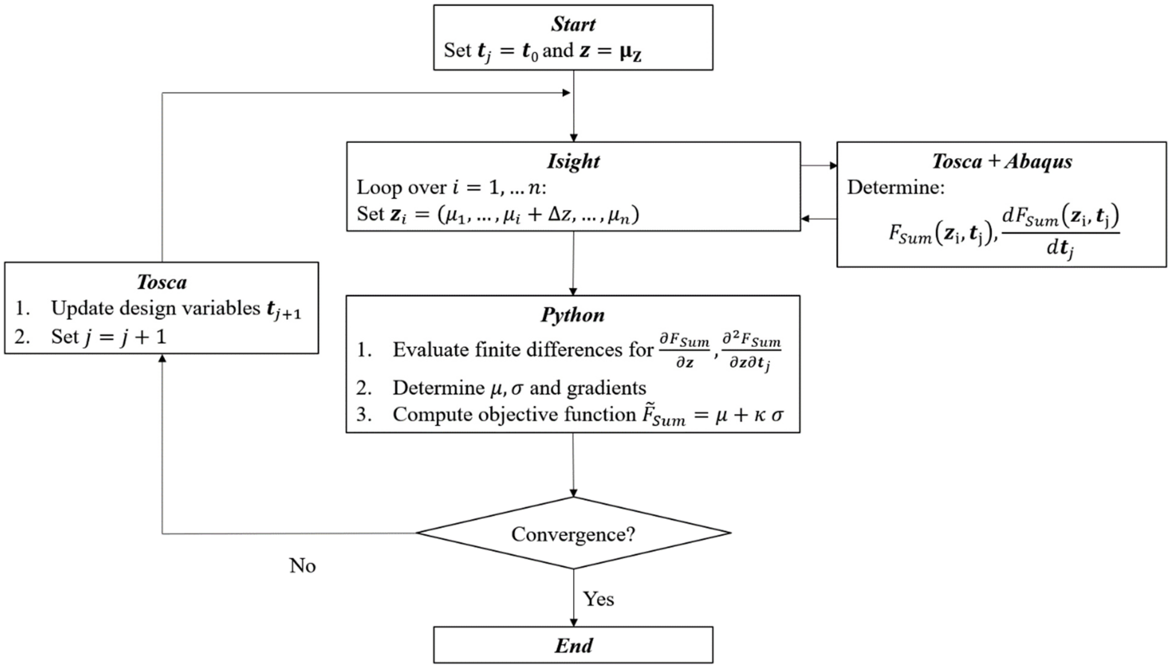

Figure 2: Optimization workflow of the numerically implemented nonintrusive approach for robust sizing optimization.

3 Finite element model of stiffened panel

The following section presents the numerical model of the stiffened panel studied in the present work. The structure was part of a previous study by Zimmermann et al. [11] and was used for probabilistic analysis by Kriegesmann [40]. The finite element model shown in Figure 3 is based upon geometrical nonlinear modeling. The geometric dimensions are listed in Table 1. The finite element mesh consists of 10’593 quadratic shell elements (S4). The mesh size is sufficiently refined for capturing the local buckling modes. Three shell sections are defined for the skin, stringer foot and stringer blade, having the initial thicknesses as listed in Table 1. The panel is fully clamped at one short edge and a prescribed displacement of u is applied at the other edge having the other five degrees of freedom constrained. Additional boundary conditions are applied to support the free edges. The corresponding edges are highlighted in red in Figure 3 and the restricted degrees of freedom are given with respect to the cylindrical coordinate system. The reaction forces resulting from the axial prescribed displacement compression are given as F.

The model consists of a linear elastic isotropic constitutive material having a Young’s modulus of $E = 70$ GPa and a Poisson’s ratio of $\nu = 0.34$. Numerical experiments applying an elastoplastic constitutive material model showed that the initial local buckling and the initiation point of the global buckling are identical for both material models. Additionally, the postbuckling deformations showed only insignificant divergences between the elastic and elastoplastic analysis subject to large displacements. These studies were performed considering both initial and optimized thickness distributions of the panel structure.

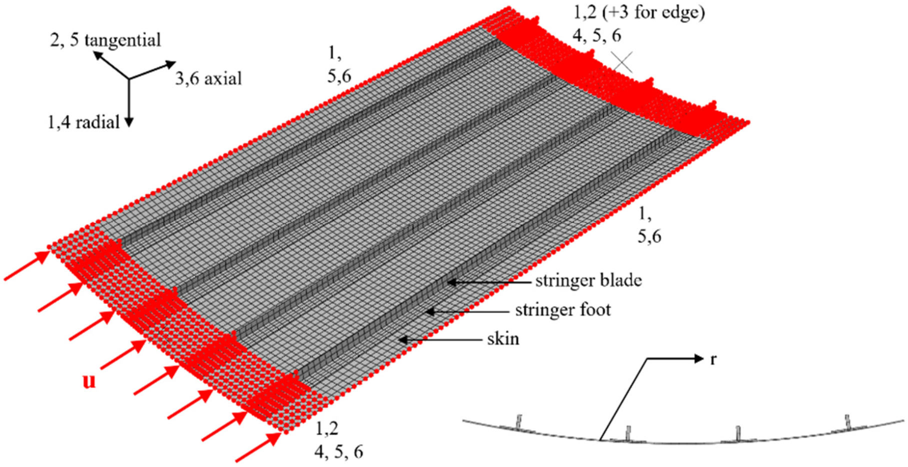

Figure 3: Discretized model of panel showing the applied boundary conditions.

Table 1: Deterministic geometric properties of panel modelled after [11]

Panel length	$l = 780$ mm
Free length (maximum buckling length)	$l_f = 660$ mm
Internal radius	$r = 1000$ mm
Internal arc length	$a = 419$ mm
Deterministic skin thickness	$t_s = 1$ mm
Deterministic stringer foot thickness	$t_f = 1.5$ mm
Deterministic stringer blade thickness	$t_b = 3$ mm
Stringer height	$h = 14$ mm
Stringer width	$f = 37.9$ mm
Distance stringer to stringer	$d = a/4$
Distance stringer to longitudinal edge	$e = a/8$

Furthermore, a number of subsets or *clustering groups* of shell elements are defined. The panel is divided into 10 sets with respect to the axial direction and 5 sets with respect to the circumferential direction, yielding a total of 50 groups for the skin as shown in Figure 4a. Each stringer is divided with respect to the axial direction as shown in Figure 4b, yielding a total of 10 groups for each stringer footing and stringer blade. A total of 80 clustering groups are defined for all four stringers. The total number of thickness design variables is 130 when considering the clustered groups. When symmetry along the middle axis with respect to the axial direction is considered, the number of clustered groups is reduced to 70, yielding 70 thickness design variables.

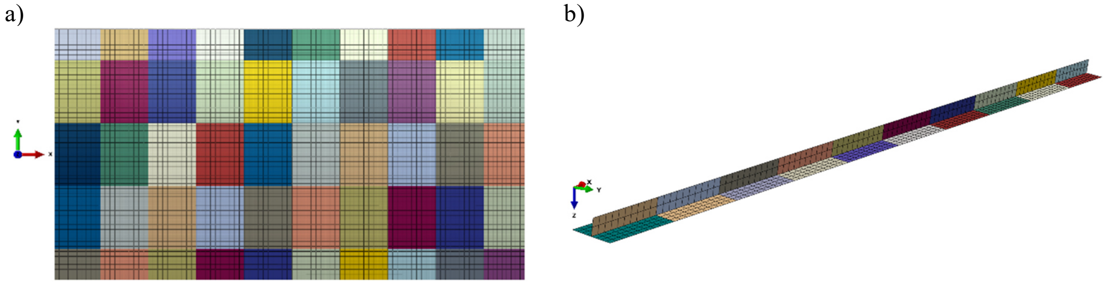

Figure 4: Visualization of the clustered groups for the thickness design variables of (a) the skin and (b) a stringer.

3.1 Geometric imperfections and buckling modes

Zimmermann [11] studied geometric imperfections of the panel skin resulting from the manufacturing of eight stiffened panels. Kriegesmann [44] parametrized these imperfections using a half-wave cosine function as shown in Eq. (15) for a probabilistic analysis of the panel structure. A total of 300 Fourier coefficients are transformed using the transformation approach presented in section 2.3.2 to 7 uncorrelated random parameters z_i having $\mu_i = 0$ and $\sigma_i = 1$. Then, a sample of Fourier coefficients $\mathbf{A}$ is derived using a random realization $\boldsymbol{z}$ and Eq. (18) for describing a realization of the geometric imperfections. Figure 5 shows three realizations for the geometric imperfections. The colored plots show the imperfection pattern $\bar{w}$ with respect to the perfect geometry following Eq. (15). The characteristic geometric imperfection mode subject to the mean Fourier coefficients $\boldsymbol{\mu}$ $(\boldsymbol{z}_i = 0)$ is referred to as *mean imperfections* for the following analyses.

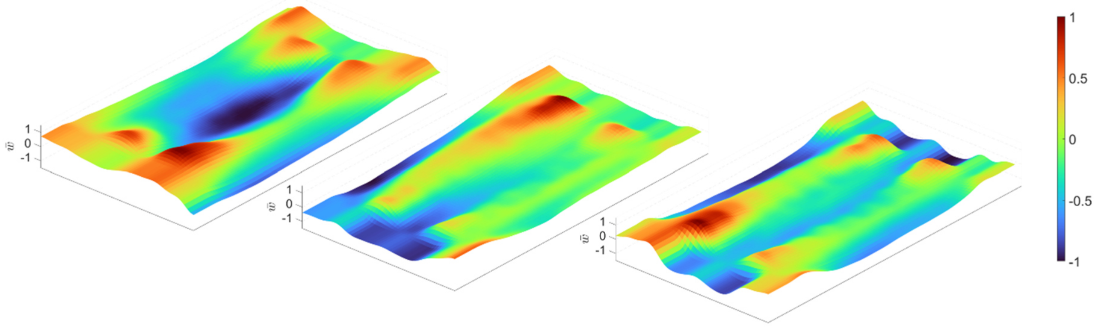

Figure 5: Random realizations of imperfection pattern $\bar{w}$ for skin geometry.

The sensitivity of the panel performance with respect to geometric imperfections is demonstrated using the force-displacement curves of two finite element analyses considering perfect and perturbed skin geometry shown in Figure 6a. At first, the structural responses of both structures under axial compression are linear and have almost indentical stiffness as dicussed in section 2.1. The reaction force drops suddenly when reaching the critical load level for global buckling $F_{Buckling}$ before the reaction force increases again as decribed in Figure 1. As expected, the global buckling load $F_{Buckling}$ is lower for the panel having a perturbed geometry.

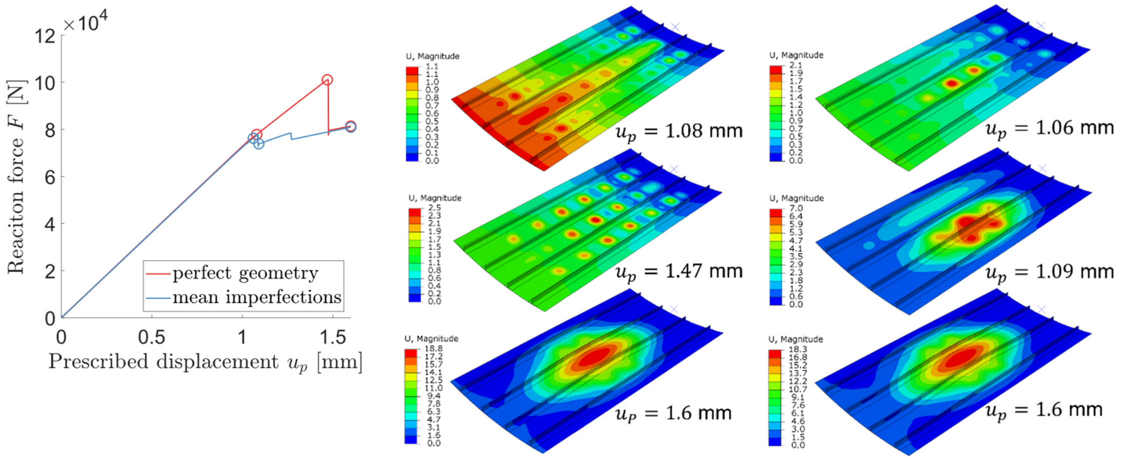
a) Force-displacement curves

b) Deformation of geometrically perfect panel

c) Deformation of panel subject to mean imperfections

Figure 6: (a) Force-displacement curves for buckling analysis of stiffened panel considering perfect geometry and mean-perturbed geometry including visualizations of initial buckling mode up to final postbuckling mode.

Both the reduced initial buckling load and the deformation modes of the panel are sensitive to geometric imperfections. Deformation patterns for the panel designs having perfect and perturbed geometry corresponding to the load-deflection curves in Figure 6a are shown in Figure 6b and Figure 6c, respectively. The different deformations shown at the top plots of Figure 6b and Figure 6c for a prescribed displacement of approximately $u_p \sim 1$mm illustrate the imperfection sensitivity of the deformation mode for the local skin buckling. The geometrically perfect panel continues to deform locally between the stringers as shown in the middle plot of Figure 6b until the onset of global buckling at a compression of $u_p \sim 1.5$mm. Then, the buckling mode transforms into the global postbuckling mode shown at the bottom of Figure 6b. In contrast, the imperfect panel reaches the global buckling point at approximately $u_p \sim 1.1$mm, shown as the middle plot in Figure 6c. The second decrease in reaction force at approximately $u_p \sim 1.3$mm corresponds to the forming of the postbuckling mode shown in the bottom of Figure 6c. This deformation is found to be the common global postbuckling mode for all of the following designs.

The panel design perturbed by the mean imperfections is selected as the reference geometry for the remaining sections of this paper due the significant impact of the geometric imperfections on the buckling load and total load-carrying capacity.

4 Results

The present section addresses the sizing optimization of a curved and stiffened panel maximizing the sum of the reaction forces over time subject to a mass constraint. Numerical experiments addressing deterministic and robust sizing optimization for buckling show the significant potential of the present quasi-static design approach. Table 2 lists all optimization formulations discussed in the following. Three setups of design variables are considered for both the deterministic and the robust design optimization: Free sizing where all element thicknesses are considered as individual design variables; clustered design variables as presented in Figure 4; and symmetrically clustered design variables considering symmetry along the center axis with respect to the axial direction. Six different optimizations are carried out in total. Firstly, section 4.1 discusses the results of the deterministic optimization. Secondly, the results of the robust design optimization are presented in section 4.2. Lastly, the designs are compared in section 4.3 with respect to the global buckling load and the stochastic moments of the reaction forces. The FOSM approximation of the stochastic moments is validated using the Monte Carlo method.

Table 2: Overview of optimizations conducted and presented in the following sections

Optimization approach	Design variables		
	Free	Clustered	Symmetrically clustered
Deterministic	Section 4.1.1	Section 4.1.2	Section 4.1.2
Robust	Section 4.2.1	Section 4.2.2	Section 4.2.2

4.1 Deterministic optimization

The following section shows deterministically optimized designs of the stiffened and curved panel using the optimization formulation presented in section 2.1. The gradient-based sizing optimization is carried out using Tosca and Abaqus. The element thicknesses are considered as design variables having the lower and upper bound values of $0.2 \times \mathbf{t}_{initial} \leq \mathbf{t} \leq 2 \times \mathbf{t}_{initial}$. The design response for the optimization objective is the sum of $I = 15$ time dependent reaction forces under axial compression for the optimization formulation in Eq. (1). Preliminary numerical experiments show that the buckling and postbuckling loads of the panel are increased significantly through the optimization. Thus, the prescribed displacement is increased to $u_p = 3.2$ mm for the following experiments.

4.1.1 Free sizing optimization

The first example presents the results of a free sizing optimization. The so-called free sizing optimization is referring to an optimization where the thickness of each element is considered as a design variable. Figure 7 shows the optimization iteration history where the optimization yields a converged design after 50 optimization iterations. The mass is redistributed, fulfilling the mass constraint $m \leq m_{initial}$, and the initial stiffness under axial compression is essentially retained. The optimized thickness distribution is shown in Figure 8b compared to the initial thickness distribution in Figure 8a. The force-displacement curves for the optimized design and the initial design are shown in Figure 8c. The time points considered for the transient reaction forces are transformed to corresponding displacements and indicated as dashed vertical lines. The reader is reminded that all designs are subject to mean imperfections as introduced in section 3.1, and the only difference between the initial design and the optimized design is the thickness distribution.

Figure 8c shows that the free sizing optimization yields a design having significantly increased buckling load by approximately 120%. Even though the buckling load is not considered directly for the specific model and optimization formulation, the approach discussed in section 2.1 is demonstrated to be numerical valid for the specific model.

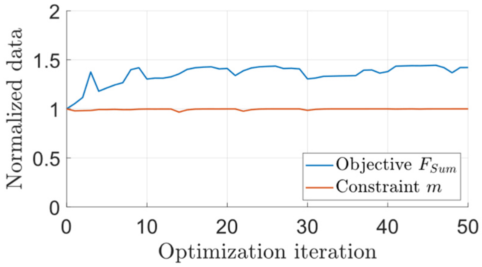

Figure 7: Optimization iteration history showing the normalized objective, which are the summarized reaction forces, and mass constraint for the deterministic sizing optimization as shown in Figure 8b.

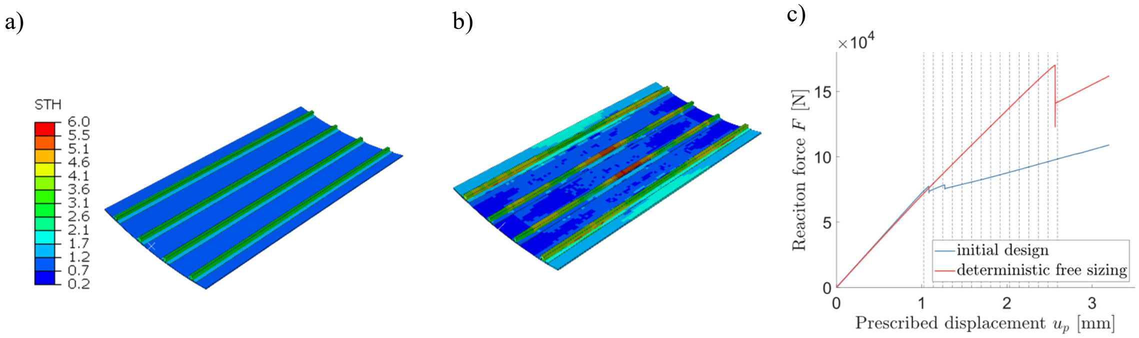

Figure 8: Thickness distributions and (c) force-displacement curves for (a) initial design and (b) deterministically optimized design for maximizing the sum of reaction forces over time.

4.1.2 Clustered design variables

Frequently, it is required to reduce the number of design variables for industrial manufactured applications by grouping or also called *clustering* the thickness design variables. Sizing optimization considering clustering of thickness design variables is discussed in e.g. [45]. Two optimization setups having clustered design variables are presented in the following section. The groups applied for the clustering of the design variables are defined and visualized in section 3. The first optimization setup considers 130 clustering groups as design variables. Symmetry of the clustering groups with respect to the center in axial direction is considered for the second optimization setup, yielding 70 design variables.

Figure 9c shows that the structural performance of the optimized designs is very similarly with respect to the global buckling load and the postbuckling behavior. The thickness distributions shown in Figure 9a and b are rather different from a symmetrical point of view but more less have the same total thickness distribution in the axial direction. The optimization for the clustered thickness design variables converges after 50 optimization iterations whereas the optimization considering the symmetrically clustered design variables converges after only 43 optimization iterations. Again, both designs show a significant increase in global buckling load by approximately 90% when compared to the reference design.

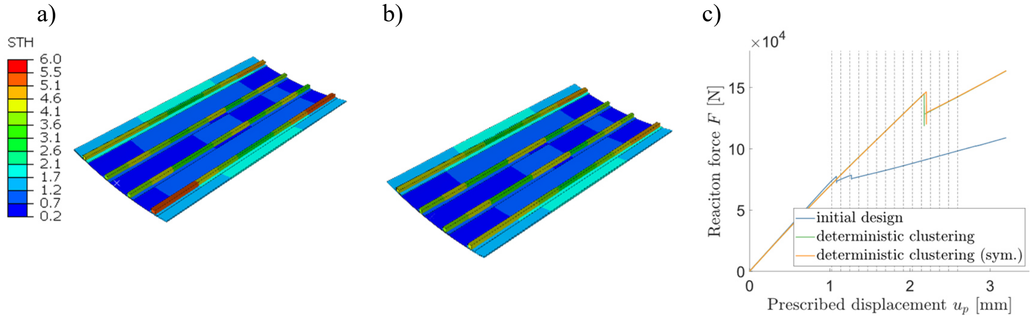

Figure 9: Optimized thickness distributions and (c) force-displacement curves for the optimized designs considering (a) clustered design variables and (b) symmetrical clustered design variables.

4.1.3 Comparison of deterministically optimized designs

Figure 10 compares the three deterministically optimized designs discussed in section 4.1.1 and 4.1.2, respectively. The three designs will be referred to as *a*, *b* and *c* corresponding to the labels in Figure 10.

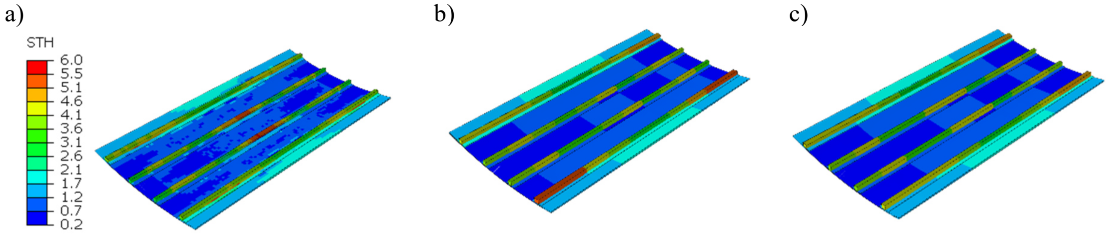

Figure 10: Shell-element thickness distribution for deterministically optimized designs considering (a) free, (b) clustered and (c) symmetrically clustered design variables.

Figure 11 shows the force-displacement curves for the three designs in Figure 10, and the numerical results are listed in Table 3. As discussed in section 4.1.2, the designs *b* and *c* considering clustered design variables have almost identical performance. Designs *b* and *c* show an increase of 35% of the objective while it is increased by 41% for design *a* compared to the initial design. This difference is expected, as the free sizing optimization has the highest degree of design freedom for the thickness design variables. Consequently, considering clustered thickness design variables constrain the design freedom and limit the potential increase in the buckling. However, for all three cases we see a significant increase in the buckling and postbuckling load carrying capacity.

At the same time the run-time for the optimization is reduced by approximately 1/3 for designs *b* and *c*. Table 3 also shows the computational runtimes for the three designs. The difference in the computational runtimes is mainly given by the number of Newton-Raphson factorizations for the direct solver when solving the structural equilibrium in Eq. (2) for each optimization iteration. Hence, if a buckling mode and postbuckling modes change from one optimization iteration to the next optimization iteration, then these two optimization iterations can have very difference computational costs. Thereby, estimating the computational costs and runtime prior to an optimization is very difficult, whereas optimization using a linear modeling for Eq. (2) having no buckling would always have the same runtime per optimization iteration.

We see that the approach for the optimization formulation outlined in section 2.1 is valid for the specific model and optimization formulation. The stiffness of the panel under axial compression before reaching global buckling is mainly determined by the total mass of the panel, that is the mass constraint value for this case. Thus, the objective function for the reaction forces can only be maximized by increasing the reaction forces in the buckling and postbuckling range, and thereby increasing the buckling load resistance implicitly. Overall, the quasi-static sizing optimization produces great results by explicitly increasing the sum of reaction forces (defined as the optimization objective) by at least 35% and implicitly increasing the global buckling load by at least 90% for the optimization setups. In the following sections the same optimization setups are examined in the context of robust design optimization considering manufacturing uncertainties.

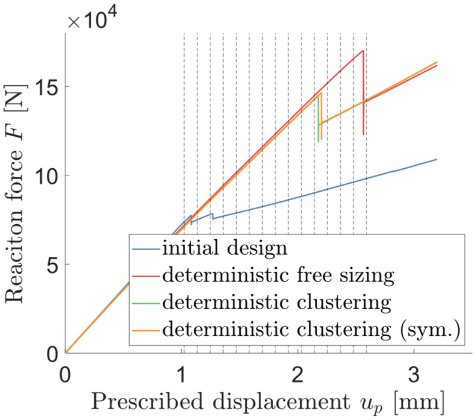

Figure 11: Force-displacement curves of panels optimized for maximal sum of reaction forces and initial design considering mean imperfections.

Table 3: Numerical results for optimization objective of deterministically optimized designs including global buckling load, number of iterations and run-time

Optimization approach	Objective $[1 \times 10^6$ N]	Buckling load $[1 \times 10^3$ N]	Iterations	Run-time
Free sizing	1.81	170	50	3d
Clustered design variables	1.73	145	50	2d 2h
Symmetrically clustered design variables	1.73	146	43	2d 1h
Initial design	1.28	78	-	-

4.2 *Robust sizing optimization for manufacturing imperfections*

The optimization setup from section 4.1 is considered for robust design optimization. The nonintrusive Taylor-based approach presented in section 2.2 is applied. The objective for deterministic optimization is the sum of transient reaction forces. Thus, the mean and standard deviation of the sum of reaction forces is considered for the robust optimization objective given in Eq. (3). The constant κ is set to $\kappa = -1$. The random parameters z_i are the seven uncorrelated parameters resulting from the transformation of the Fourier coefficients presented in section 2.3.2 and introduced for the panel structure in section 3.1. The stochastic moments of the random parameters are $\mu_{z_i} = 0$ and $\sigma_{z_i} = 1$. The step size for the finite differences in Eqs. (13) and (14) is $\Delta z_i = 1.5$.

4.2.1 Free sizing optimization

The first optimization setup for a robust free sizing optimization corresponds to the deterministic optimization setup discussed in section 4.1.1 except from including the uncertainties given in section

2.3 and using the optimization formulation in Eq. (3). The optimization yields a converged design after 57 optimization iterations. Figure 12 shows the iteration history and indicates a smooth optimization convergence even when the quasi-static optimization is combined with the nonintrusive approach for robust design optimization.

When comparing Figure 7 for the convergence of the deterministic optimization to Figure 12 showing the convergence of the robust optimization then surprisingly, the robust optimization is smoother in convergence than the deterministic optimization. Thus, the assumption for the present example and other numerical experiments is that the buckling optimization is highly nonconvex with many local minima. The uncertainties for the robust optimization formulation eliminate many of these local minima present in the deterministic optimization as well as leading to a flat minimum being more robust than the sharp minimum obtained in the deterministic optimization.

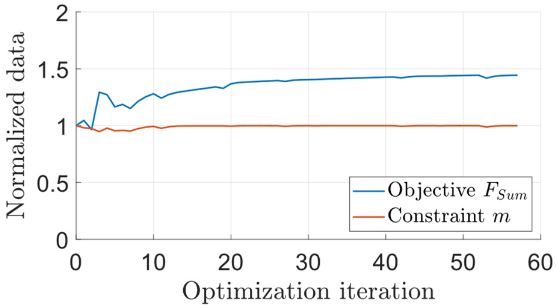

Figure 12: Optimization iteration history showing the normalized objective, which are the summarized reaction forces, and mass constraint of the free robust sizing optimization shown in Figure 13b.

The robust optimized shell thickness distribution shown in Figure 13b differs from the deterministically optimized design shown in Figure 13a. The thickness increase in the middle of the two inner stringers is more pronounced for the robust design. Furthermore, the robust optimization shifts material to the ends of one of the outer stringers and thereby, effectively reducing the critical length of the stringer. Having more material at the stringers instead of at the skin leads to an early onset of local skin buckling which is not of concern for the present studies as the global buckling load is maximized. However, as also discussed when comparing the convergence of the deterministic optimization (Figure 7) and the robust optimization (Figure 12), the comparison of the force-displacement curves in Figure 13c of the optimized designs shows that the global buckling load of the robust optimized design is even higher than for the deterministically optimized design when considering the mean perturbation modes for the geometric imperfections. Simultaneously, the axial stiffness for the robust design decreases only slightly compared to the deterministically optimized design due to the early onset of local buckling in the skin and the bending moments that are thereby introduced.

The comparison of the robust optimized design with the initial design shows a significant increase of the global buckling load by approximately 150% for the same mass. Accordingly, the conclusion is again that many of the local minima present in the deterministic optimization are eliminated in the robust formulation yielding a higher buckling load than the deterministic optimization when analyzed for the mean perturbation modes for the geometric imperfections.

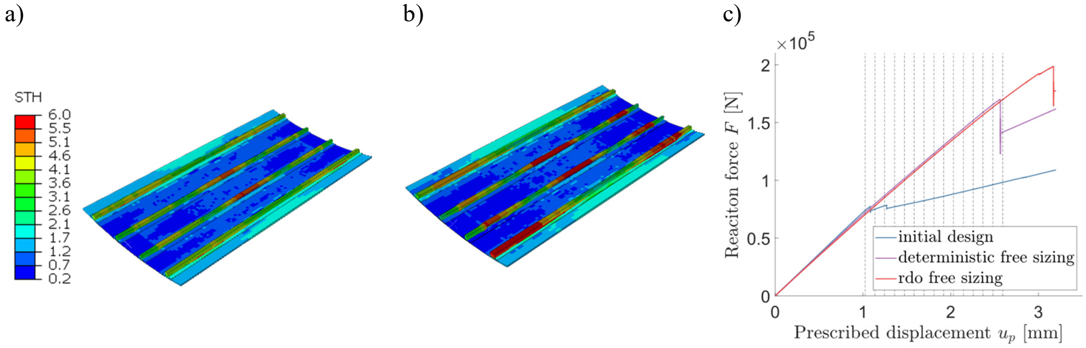

Figure 13: Thickness distributions for (a) the deterministically optimized design and (b) the robust optimized design for maximizing the sum of reaction forces over time and (c) corresponding force-displacement curves.

4.2.2 *Clustered design variables*

Following the methodology of section 4.1, the same clustering setups for the design variables are applied to robust design optimization.

The robust optimized designs shown in Figure 14a and Figure 14b have significantly different optimized thickness distributions compared to the deterministically optimized designs shown in Figure 9. The optimization considering clustered design variables without symmetry-constraints yields a design that does not reach buckling when subject to the mean geometric imperfections and a maximum prescribed axial displacement of $u_p = 3.2$mm. Hence, the maximum prescribed axial displacement for the finite element analysis is increased to $u_p = 6.4$mm for the following discussions. The stiffness of the design starts to decrease in the prebuckling deformation range due to increasing bending moments for a prescribed axial displacement of approximately $u_p \approx 1.5$mm. Figure 15a shows the deformation mode at $u_p = 3.2$mm where the panel deforms outwards in the radial direction. Nonetheless, the global buckling after a snap-through from prebuckling to postbuckling has the same deformation mode shown in Figure 15b as the postbuckling mode for previous designs shown in Figure 6b-c. Additionally, the buckling load value is approximately 250% higher than the buckling load for the initial design and 40% higher than for the optimized design resulting from robust free sizing optimization. Again, this can only be explained with the optimized design resulting from robust free sizing optimization being a local minimum.

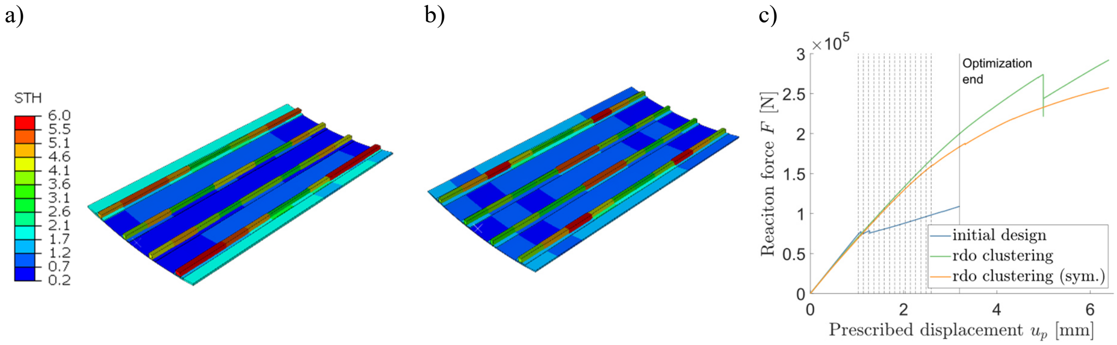

Figure 14: Optimized thickness distributions for the robust optimized designs considering (a) clustered design variables and (b) symmetrically clustered design variables and (c) corresponding force-displacement curves.

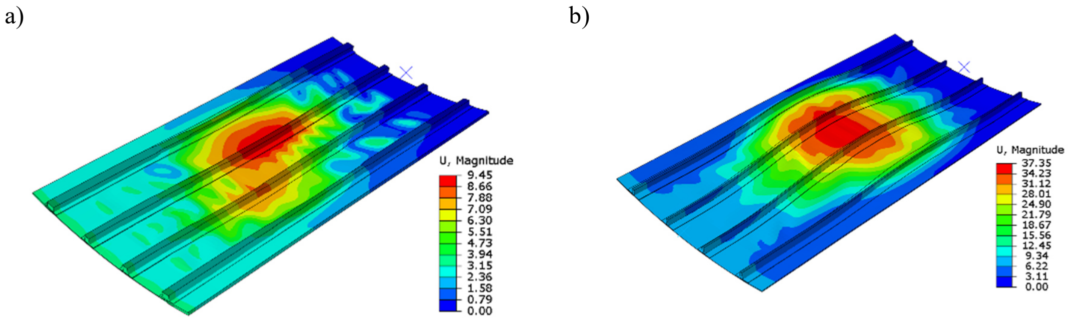

Figure 15: Deformation modes subject to a prescribed displacement of (a) $u_P = 3.2$mm and (b) $u_p = 6.4$mm of the robust optimized design considering clustered design variables as shown in Figure 14a.

The optimized panel design shown in Figure 14b is the result of the robust sizing optimization considering symmetrically clustered design variables with respect to the center axis in the axial direction. In contrast to all previously optimized designs, the force-displacement curve for this design displayed in Figure 14c lacks the characteristic drop in reaction force caused by global buckling. Instead, the stiffness of the optimized design decreases continuously for a prescribed displacement $u_p \geq 1.5$mm. From this point onwards, the deformation mode resembles qualitatively the deformation pattern shown in Figure 16a except for the differences in the actual magnitudes of the displacements. The panel deforms in the radially outward direction until the maximum prescribed displacement is reached without transforming to the postbuckling mode as observed for the previous designs. Frequently, in industrial applications such a continuous deformation behavior for the structural response is anticipated as the deformation is controlled, having no sudden buckling for all given manufacturing imperfections. However, as previously stressed such an overall structural deformation behavior in compression reaches a lower stiffness compared the other designs for their prebuckling deformation range.

All of the robust optimized designs emphasize that the optimization problem is highly nonlinear and generally sensitive to geometric perfections. The optimization system has a likelihood of converging to a different local minimum based on the gradients of the panel designs subject to arbitrary geometrical manufacturing imperfections. Nevertheless, the numerical experiments for the present application show that the robust designs have a much better performance in contrast to the deterministically optimized design just being subject to the mean imperfections during the optimization. The actual stochastic performance is analyzed in the next section for all optimized designs.

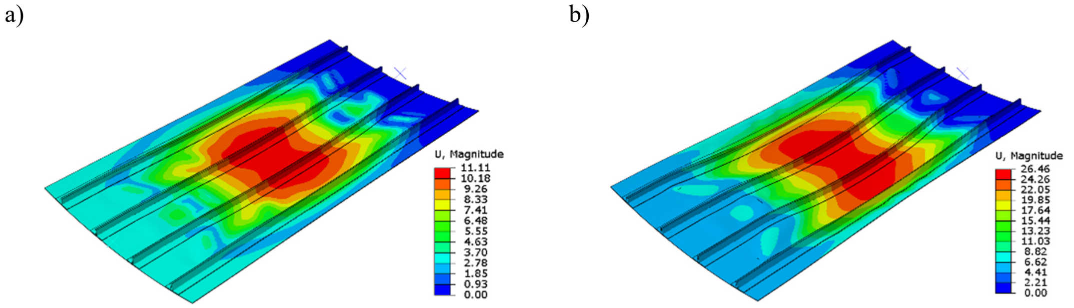

Figure 16: Deformation modes subject to a prescribed displacement of (a) $u_P = 3.2$mm and (b) $u_p = 6.4$mm of robust optimized design considering symmetrically clustered design variables as shown in Figure 14b.

4.3 Probabilistic validation and comparison of optimized designs

Six different optimized designs are presented in the previous sections 4.1 and 4.2. The three optimization setups for the design variables (free sizing, clustering, symmetric clustering) are optimized using deterministic and robust design approaches. The optimized designs have been discussed separately with respect to the thickness distribution and their characteristic force-displacement curves. The force-displacement curves are summarized in Figure 17. The present section compares the designs resulting from deterministic and robust optimization and elaborates on the probabilistic performance of optimized designs for the stiffened panel subject to scattered geometric imperfections.

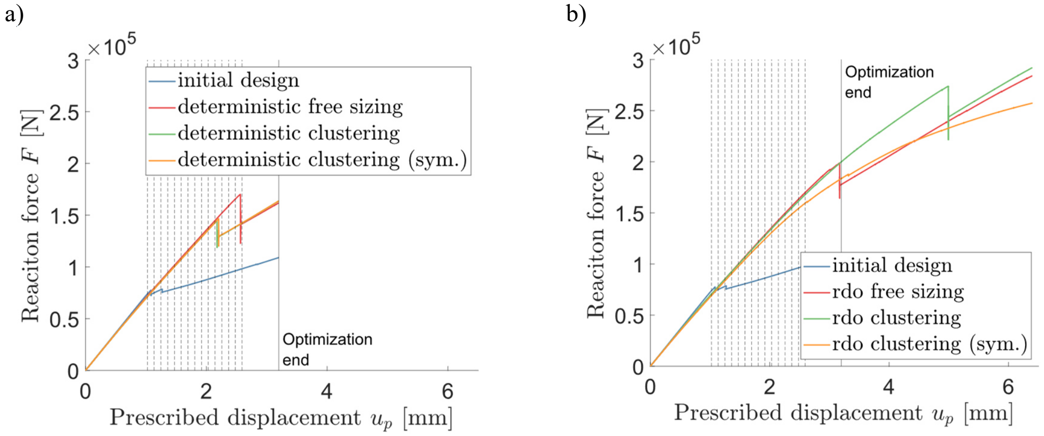

Figure 17: Force-displacement curves for (a) all deterministically and (b) robust optimized designs subject to the mean geometrical imperfections and a maximum prescribed axial compression of $u_p = 6.4$mm.

Generally, each design resulting from robust design optimization has a higher load carrying capacity than the deterministically optimized designs as shown in Figure 17. The global buckling point is higher than for all of the deterministically optimized designs. Only the robust optimized design considering symmetrically clustered design variables lacks the characteristic buckling point in the reaction force loading curve.

The robust design optimization applies the first-order second-moment method (FOSM) for an estimation of the mean value μ and standard deviation σ of F_{Sum}. A Monte Carlo simulation considering 250 realizations of the geometrical imperfections is performed for each design for validating the probabilistic results used in the robust optimization. The numerical results for the probabilistic analyses using FOSM and the Monte Carlo validation are presented in Table 4. The FOSM approximation of the mean value is accurate for most of the estimations. Deviations from the Monte Carlo validation are of practically acceptable scale. The standard deviation is overestimated by approximately a factor of two. However, the Monte Carlo simulations confirm that the variability of the objective function is significantly reduced by the RDO approach except for symmetric clustering. Hence, the FOSM approximation guides the optimization to a more robust design despite the deviation of σ.

Overall, the combination of robust design optimization with quasi-static sizing optimization considering free and clustered design variables yields designs having a significantly increased robustness subject to the geometrical imperfections. Also, the mean performance is increased, as the only improvement with respect to the initial design can occur in the postbuckling range and thereby, effectively increasing the buckling load by increasing the point of the prescribed axial displacement for which buckling appears. The global buckling loads of all designs are determined during postprocessing of the optimization results and are shown in Table 5. For that, the first limit point (or snap-through point) is considered as the global buckling load. Overall, the numerical experiments validate the assumption outlined in section 2.1 that by maximizing the sum of reaction forces, the buckling load is increased even though the buckling point is not directly included in the optimization problem formulation.

Table 4: Probabilistic analysis of the objective function F_{Sum} using FOSM and the validation of the values approximated FOSM using Monte Carlo simulation

Optimization	FOSM [1×10^6 N]			Monte Carlo [1×10^6 N]		
	μ	σ	$\mu-\sigma$	μ	σ	$\mu-\sigma$
Deterministic free sizing	1.81	0.11	1.70	1.76	0.07	1.68
Robust free sizing	1.81	0.02	1.79	1.80	0.01	1.79
Deterministic clustering	1.73	0.13	1.60	1.74	0.07	1.67
Robust clustering	1.80	0.01	1.79	1.80	0.01	1.79
Det. clustering (sym.)	1.73	0.13	1.60	1.74	0.07	1.67
Robust clustering (sym.)	1.75	0.11	1.64	1.69	0.07	1.62

Table 5: Deterministic buckling loads as well as mean values and standard deviations of buckling load for the optimized panel designs

Optimization	Buckling load [1×10^3 N]	$\mu_{F_{Buckling}}$ [1×10^3 N]	$\sigma_{F_{Buckling}}$ [1×10^3 N]
Deterministic free sizing	170	143	29
Robust free sizing	198	168	13
Deterministic clustering	145	135	24
Robust clustering	274	158	6
Det. clustering (sym.)	146	128	20
Robust clustering (sym.)	188	119	14

The results of the probabilistic analyses of the deterministically and robust free sizing optimized designs are shown in Figure 18a and Figure 18b, respectively. Each red colored curve shows a single analyzed sample in the Monte Carlo simulation. Additionally, the black curve shows the analysis of the optimized design subject to the deterministic geometric imperfections. The grey curves are composed from the mean values and standard deviations determined by either Monte Carlo or FOSM to show the estimated mean and "mean $\pm$ standard deviation" performance. For FOSM, the mean curve coincides with the deterministic analysis according to Eq. (8).

First of all, the set of red curves resulting from the Monte Carlo simulations show that there are primarily two equilibrium paths for the optimized designs. The geometric imperfections influence the onset of global buckling, i.e. the prescribed displacement for which the load drops from the prebuckling path to a postbuckling path having a lower reaction force level. In comparison to Figure 18a, the plots for the robust optimized design in Figure 18b demonstrate that the robust optimization approach from section 2.2 increases the buckling point by pushing the point upwards on the prebuckling path. Furthermore, the two equilibrium paths move closer to each other since robustness optimization rewards a reduction of the standard deviation, which corresponds to reduced imperfection sensitivity. The force-displacement curves for the designs considering clustered design variables are included in Appendix A and support the previous conclusions.

The robust optimized design considering symmetrically clustered design variables represents a similar local minimum as the deterministic optimization, as the numerical results in Table 4 indicate. Hence, the force-displacement curves given in Appendix A for this case do not show the same improvement in performance as the other two parameterization approaches. Nevertheless, they are shown for the sake of completeness and transparency.

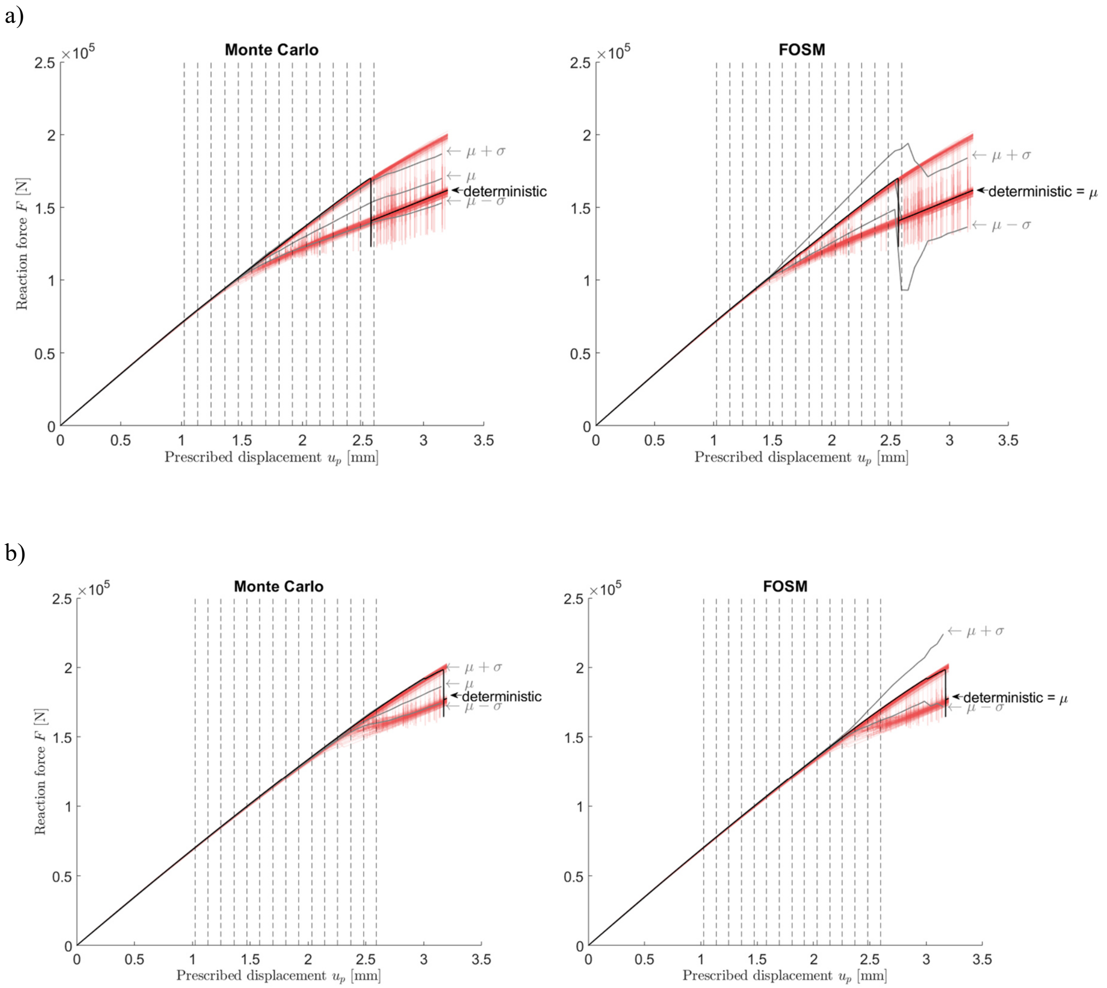

Figure 18: Force-displacement curves for the probabilistic analysis using FOSM and validation using Monte Carlo simulation (red lines) of the free-sizing optimized designs for (a) deterministic optimization and (b) robust optimization.

The load-displacement curves in Figure 18 show that the Monte Carlo simulation estimates a mean path which is not followed by any realization. In fact, each realization has a reaction force higher than the mean value until global buckling and afterwards a lower reaction force. When considering the reaction force at one certain displacement, for example u_p = 3mm, the distribution of this reaction force is a bimodal distribution. This observation does not allow to directly deduce that the distribution of the objective function F_{Sum} and the buckling load $F_{Buckling}$ is also bimodal. However, the histograms shown in Figure 19 reveal that F_{Sum} and $F_{Buckling}$ of the deterministically optimized panel indeed have distinct bimodal distributions. The realizations not showing a distinct limit point are not part of the histograms.

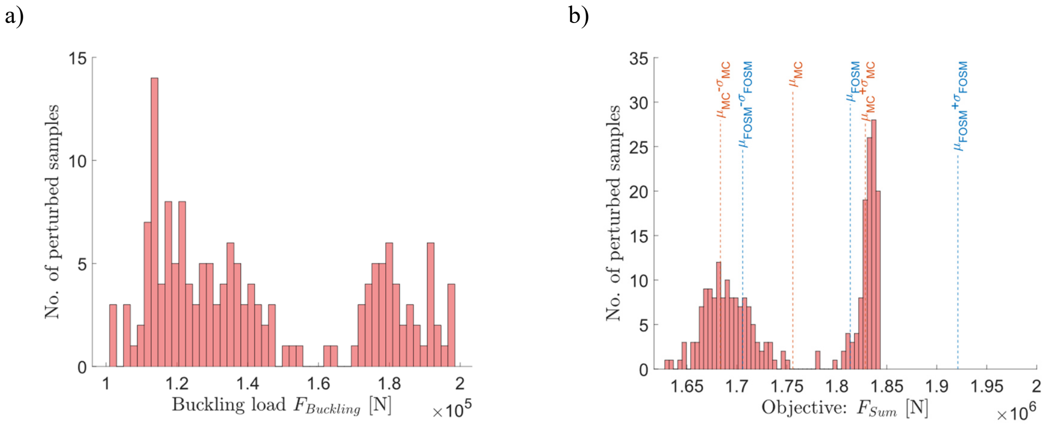

Figure 19: Histograms for (a) the global buckling load and (b) the objective function obtained using Monte Carlo simulation for deterministic optimized design.

The FOSM method does not require assumptions about the type of distribution of the objective value. However, the fact that the unimodal input distributions yield bimodal output distributions shows the nonlinearity of the function with respect to the random parameters. For the robust design the distribution of both buckling load and sum of reaction forces becomes unimodal as shown in Figure 20. The scatter of the reaction forces decreases as already seen from the standard deviations in Table 4 and Table 5, and the results of FOSM and Monte Carlo compare significantly better. The same behavior is observed for the optimized design using clustering as shown in Figure 23 in Appendix A. Again, the difference between the deterministic and the robust optimized designs considering symmetric clustering of thickness design variables is negligible.

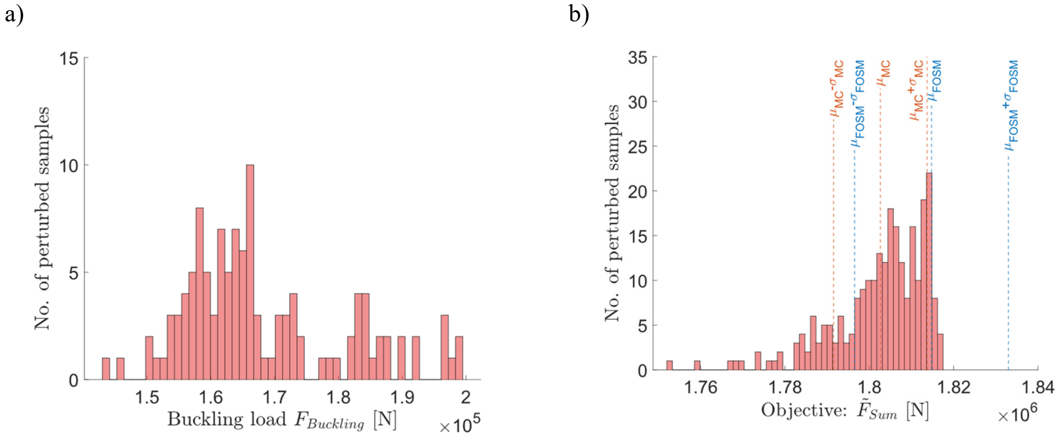

Figure 20: Histograms for (a) the global buckling load and (b) the optimization objective derived from Monte Carlo simulation for robust optimized design.

5 Conclusions

A new numerical approach for deterministic and robust thickness sizing optimization of global buckling resistance is presented. The numerical experiments are performed for an axially compressed curved and stiffened panel. The panel is a use case of a design being sensitive to manufacturing uncertainties in the form of geometrical imperfections. Nonlinear quasi-static finite element analyses in time using backward Euler integration determine the reaction forces in the pre- and postbuckling range for prescribed displacements.

The deterministic optimization formulation primarily maximizes the reaction forces at predefined prescribed displacements in the pre- and postbuckling range. Implicitly, this leads to a maximization of the global buckling load while neglecting local buckling. The robust sizing optimization approach maximizes the mean and minimizes the standard deviation of reaction forces with respect to the manufacturing imperfections using the first-order second-moment (FOSM) method. The numerical implementation combines existing derivatives with respect to the design variables and the derivatives with respect to the manufacturing imperfections using finite differences. The resulting nonintrusive approach can be implemented with any existing software for deterministic structural optimization.

The results for the thickness optimized panels show that the manufacturing uncertainties are of practical concern when maximizing the buckling resistance. The optimized panels have the same mass as the initial design while having a buckling load almost twice the reference values or even more when compared to the buckling load of the initial design subject to mean imperfections. Simultaneously, these designs also have a significantly improved robustness against geometric imperfections.

The results obtained using the FOSM method are validated using Monte Carlo simulations showing an appropriate agreement. More essentially, the Monte Carlo results confirm that the use of FOSM in the robust sizing optimization indeed drives the optimizer to a considerably more robust design.

Additionally, we observe that sizing buckling optimization has many local minima. Interestingly, the consideration of uncertainties for robust optimization compared to the deterministic optimization often eliminates many of these local minima. Thereby, the robust buckling optimized designs frequently have a higher buckling load than deterministically optimized designs when subject to the mean geometric imperfections.

Acknowledgements

Parts of the work presented supported through the program Calls for Transfer (reference number C4T532) funded by the Behörde für Wissenschaft, Forschung, Gleichstellung und Bezirke der Freien und Hansestadt Hamburg (BWFGB). The financial support is gratefully acknowledged.

Appendix A

This section presents the probabilistic force-displacement curves as introduced in section 4.3 for the deterministic and robust optimization considering the clustered design variables.

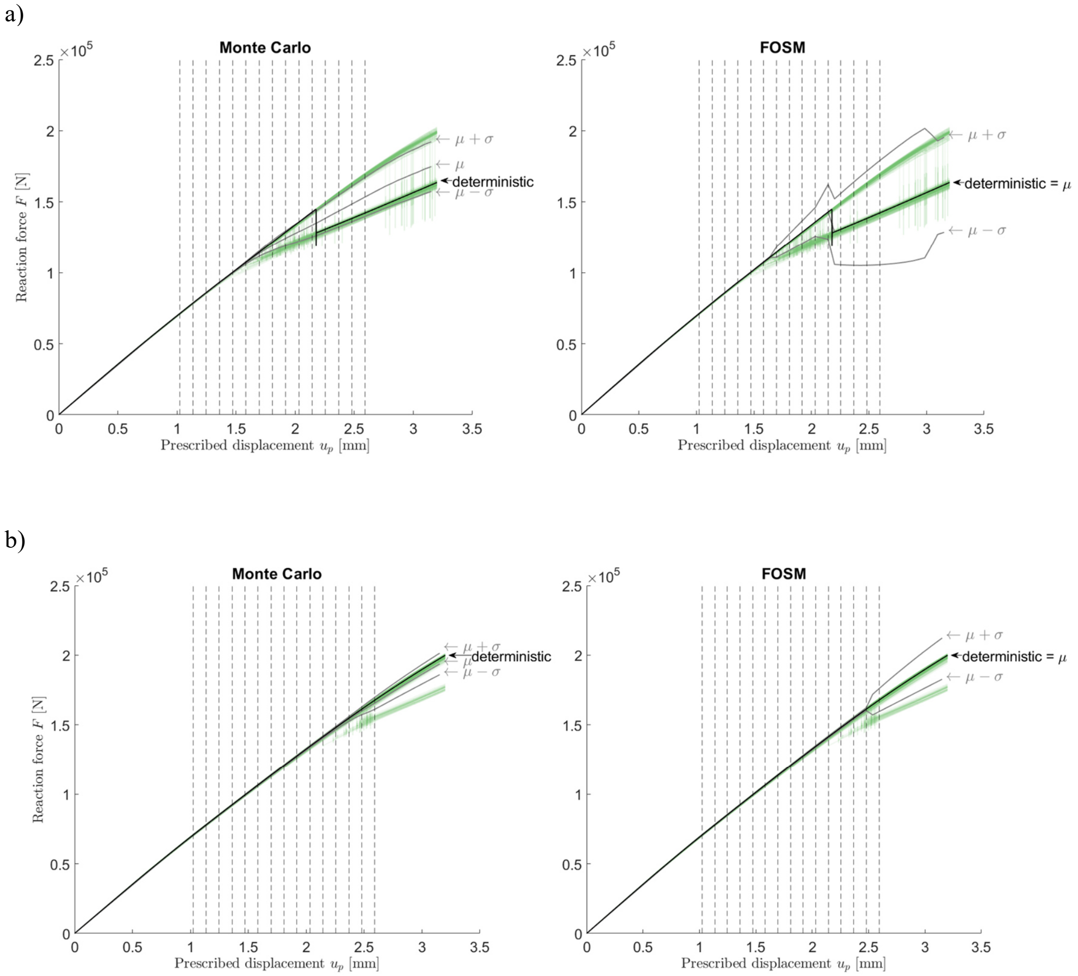

Figure 21: Force-displacement curves for (a) deterministically and (b) robust optimized design considering clustered design variables analyzed using FOSM and validated using a Monte Carlo simulation.

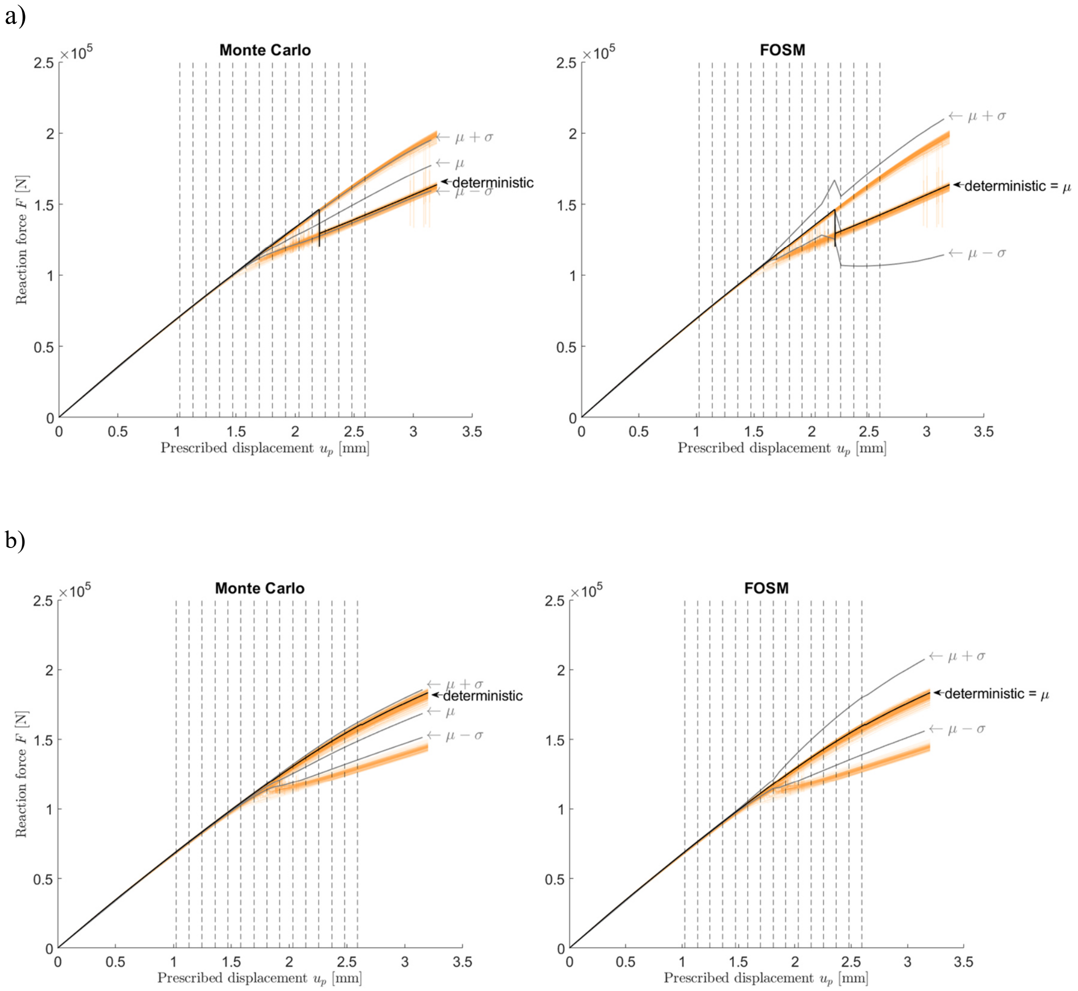

Figure 22: Force-displacement curves for (a) deterministically and (b) robust optimized design considering symmetrically clustered design variables analyzed using FOSM and validated using a Monte Carlo simulation.

The following figures show the histograms for the sum of reactions forces for the optimized design using clustering and symmetric clustering.

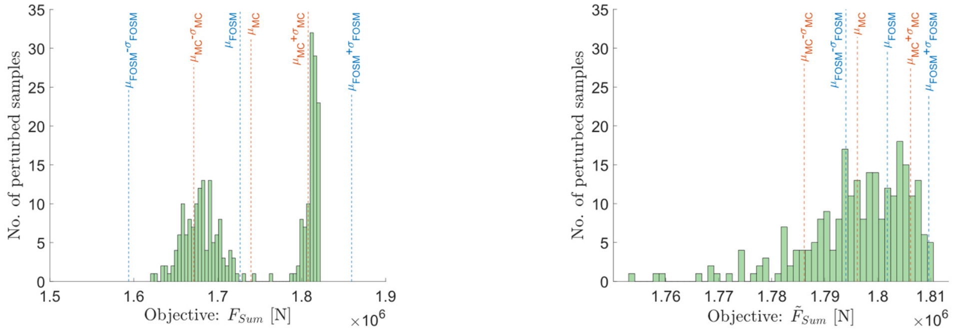

a) deterministic clustering

b) robust clustering

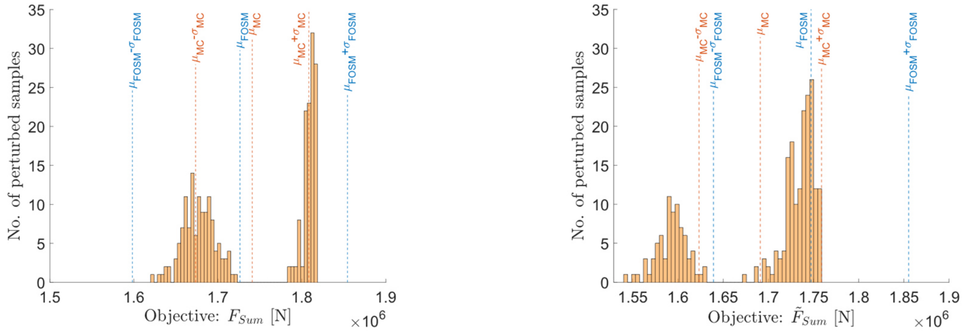

c) deterministic symmetric clustering

d) robust symmetric clustering

Figure 23: Histograms for optimization objective for designs considering clustered thickness design variables (a-b) and symmetrically clustered thickness design variables (c-d).

References

[1] W. T. Koiter, "On the Stability of Elastic Equilibrium," NASA, NASA-TT-F-10833, 1967.

[2] J. Singer, T. Weller, and J. Arbocz, *Buckling Experiments: Experimental Methods in Buckling of Thin-Walled Structures*, vol. 1. Wiley, New York, 1997.

[3] "Buckling of Thin-Walled Circular Cylinders," NASA, NASA SP-8007, 1968.

[4] J. Arbocz, "Future Directions and Challenges in Shell Stability," 1997, vol. AIAA Paper 97-1077, pp. 1949–1962.

[5] J. Arbocz, J. H. Starnes, and M. P. Nemeth, "Towards a Probabilistic Criterion for Preliminary Shell Design," *AIAA-98-2051*, pp. 2941–2955, 1998.

[6] I. Elishakoff, S. van Manen, P. G. Vermeulen, and J. Arbocz, "First-Order Second-Moment Analysis of the Buckling of Shells with Random Imperfections," *AIAA journal*, vol. 25, no. 8, pp. 1113–1117, 1987.

[7] B. Kriegesmann, R. Rolfes, C. Hühne, and A. Kling, "Fast Probabilistic Design Procedure for Axially Compressed Composite Cylinders," *Composites Structures*, vol. 93, pp. 3140–3149, 2011, doi: 10.1016/j.compstruct.2011.06.017.

[8] B. Kriegesmann, R. Rolfes, E. L. Jansen, I. Elishakoff, C. Hühne, and A. Kling, "Design Optimization of Composite Cylindrical Shells under Uncertainty," *Computers, Materials, & Continua*, vol. 32, no. 3, pp. 177–200, 2012, doi: 10.3970/cmc.2012.032.177.

[9] G.-J. Park, T.-H. Lee, K. H. Lee, and K.-H. Hwang, "Robust Design: An Overview," *AIAA Journal*, vol. 44, no. 1, pp. 181–191, 2006, doi: 10.2514/1.13639.

[10] G. I. Schuëller and H. A. Jensen, “Computational methods in optimization considering uncertainties – An overview,” *Computer Methods in Applied Mechanics and Engineering*, vol. 198, no. 1, pp. 2–13, Nov. 2008, doi: 10.1016/j.cma.2008.05.004.

[11] R. Zimmermann, H. Klein, and A. Kling, “Buckling and Postbuckling of Stringer Stiffened Fibre Composite Curved Panels-Tests and Computations,” *Composite Structures*, vol. 73, no. 2, pp. 150–161, 2006.

[12] L. Lamberti, S. Venkataraman, R. T. Haftka, and T. F. Johnson, “Preliminary design optimization of stiffened panels using approximate analysis models,” *International Journal for Numerical Methods in Engineering*, vol. 57, no. 10, pp. 1351–1380, 2003, doi: 10.1002/nme.781.

[13] C. Fleury, M. Bruyneel, B. Colson, and A. Remouchamps, “Buckling optimization of composite stiffened panels: some important issues,” Lisbon, Portugal, Sep. 2010.

[14] X. Qu and R. T. Haftka, “Reliability-based design optimization of stiffened panels,” in *Fourth International Symposium on Uncertainty Modeling and Analysis, 2003. ISUMA 2003.*, Sep. 2003, pp. 292–297. doi: 10.1109/ISUMA.2003.1236176.

[15] O. Bacarreza, M. H. Aliabadi, and A. Apicella, “Robust design and optimization of composite stiffened panels in post-buckling,” *Struct Multidisc Optim*, vol. 51, no. 2, pp. 409–422, Feb. 2015, doi: 10.1007/s00158-014-1136-5.

[16] Z. Meng, P. Hao, G. Li, B. Wang, and K. Zhang, “Non-probabilistic reliability-based design optimization of stiffened shells under buckling constraint,” *Thin-Walled Structures*, vol. 94, pp. 325–333, Sep. 2015, doi: 10.1016/j.tws.2015.04.031.

[17] Z. Meng, Z. Zhang, H. Zhou, H. Chen, and B. Yu, “Robust design optimization of imperfect stiffened shells using an active learning method and a hybrid surrogate model,” *Engineering Optimization*, vol. 52, no. 12, pp. 2044–2061, Dec. 2020, doi: 10.1080/0305215X.2019.1702978.

[18] C. López, O. Bacarreza, A. Baldomir, S. Hernández, and M. H. Ferri Aliabadi, “Reliability-based design optimization of composite stiffened panels in post-buckling regime,” *Struct Multidisc Optim*, vol. 55, no. 3, pp. 1121–1141, Mar. 2017, doi: 10.1007/s00158-016-1568-1.

[19] B. Kriegesmann, E. L. Jansen, and R. Rolfes, “Reliability Based Design Optimization of Stiffened Composite Panels,” in *MAAXIMUS - More Affordable Aircraft through Extended, Integrated and Mature Numerical Sizing*, R. Herrmann, Ed. Springer, 2020. [Online]. Available: http://www.springer.com/de/book/9783319489490

[20] O. Sigmund, “On the usefulness of non-gradient approaches in topology optimization,” *Struct Multidisc Optim*, vol. 43, no. 5, pp. 589–596, May 2011, doi: 10.1007/s00158-011-0638-7.

[21] I. Doltsinis and Z. Kang, “Robust design of structures using optimization methods,” *Computer Methods in Applied Mechanics and Engineering*, vol. 193, no. 23, pp. 2221–2237, Jun. 2004, doi: 10.1016/j.cma.2003.12.055.

[22] I. Doltsinis, Z. Kang, and G. Cheng, “Robust design of non-linear structures using optimization methods,” *Computer Methods in Applied Mechanics and Engineering*, vol. 194, no. 12, pp. 1779–1795, Apr. 2005, doi: 10.1016/j.cma.2004.02.027.

[23] B. Kriegesmann and J. K. Lüdeker, “Robust compliance topology optimization using the first-order second-moment method,” *Struct Multidisc Optim*, vol. 60, no. 1, pp. 269–286, Jul. 2019, doi: 10.1007/s00158-019-02216-8.

[24] M. Kleiber, T. D. Hien, H. Antunez, and P. Kowalczyk, *Parameter sensitivity in nonlinear mechanics: theory and finite element computations*. Chichester [England]; New York: John Wiley, 1997. Accessed: Sep. 20, 2018. [Online]. Available: http://search.ebscohost.com/login.aspx?direct=true&scope=site&db=nlebk&db=nlabk&AN=17910

[25] P. Michaleris, D. A. Tortorelli, and C. A. Vidal, “Tangent operators and design sensitivity formulations for transient non-linear coupled problems with applications to elastoplasticity,” *Int. J. Numer. Meth. Engng.*, vol. 37, no. 14, pp. 2471–2499, Jul. 1994, doi: 10.1002/nme.1620371408.

[26] K. Steltner, C. B. W. Pedersen, and B. Kriegesmann, “Non-intrusive approach for stiffness and strength topology optimization under uncertainty,” *submitted for publication*, 2021.

[27] C. B. W. Pedersen, “Topology optimization design of crushed 2D-frames for desired energy absorption history,” *Struct Multidisc Optim*, vol. 25, no. 5–6, pp. 368–382, Dec. 2003, doi: 10.1007/s00158-003-0282-y.

[28] H. M. Hilber, T. J. R. Hughes, and R. L. Taylor, “Improved numerical dissipation for time integration algorithms in structural dynamics,” *Earthquake Engineering & Structural Dynamics*, vol. 5, no. 3, pp. 283–292, 1977, doi: 10.1002/eqe.4290050306.

[29] T. Liu, C. Zhao, Q. Li, and L. Zhang, “An efficient backward Euler time-integration method for nonlinear dynamic analysis of structures,” *Computers & Structures*, vol. s 106–107, pp. 20–28, Sep. 2012, doi: 10.1016/j.compstruc.2012.03.019.

[30] *Abaqus*. Dassault Systèmes, 2021. [Online]. Available: www.simulia.com

[31] C. B. W. Pedersen, S. Kulathu, S. Mulmule, P. Upadhyay, and K. Bose, “Conceptual Crashworthiness Sheet Sizing,” presented at the 14th World Congress on Structural and Multidisciplinary Optimization, WCSMO 14, Online, Jun. 2021.

[32] J. S. Jensen, P. B. Nakshatrala, and D. A. Tortorelli, “On the consistency of adjoint sensitivity analysis for structural optimization of linear dynamic problems,” *Struct Multidisc Optim*, vol. 49, no. 5, pp. 831–837, May 2014, doi: 10.1007/s00158-013-1024-4.

[33] A. Haldar and S. Mahadevan, *Probability, Reliability and Statistical Methods in Engineering Design*, 1. Auflage. New York ; Chichester England: John Wiley & Sons, 1999.

[34] B. Sudret, S. Marelli, and J. Wiart, “Surrogate models for uncertainty quantification: An overview,” in *2017 11th European Conference on Antennas and Propagation (EUCAP)*, Mar. 2017, pp. 793–797. doi: 10.23919/EuCAP.2017.7928679.

[35] S. Krumscheid, F. Nobile, and M. Pisaroni, “Quantifying uncertain system outputs via the multilevel Monte Carlo method — Part I: Central moment estimation,” *Journal of Computational Physics*, vol. 414, p. 109466, Aug. 2020, doi: 10.1016/j.jcp.2020.109466.

[36] E. M. Papoutsis-Kiachagias, D. I. Papadimitriou, and K. C. Giannakoglou, “Robust design in aerodynamics using third-order sensitivity analysis based on discrete adjoint. Application to quasi-1D flows,” *International Journal for Numerical Methods in Fluids*, vol. 69, no. 3, pp. 691–709, 2012, doi: 10.1002/fld.2604.

[37] B. S. Lazarov, M. Schevenels, and O. Sigmund, “Topology optimization with geometric uncertainties by perturbation techniques,” *Int. J. Numer. Meth. Engng*, vol. 90, no. 11, pp. 1321–1336, 2012, doi: 10.1002/nme.3361.

[38] J. Arbocz, “Past, Present and Future of Shell Stability Analysis,” *Zeitschrift für Flugwissenschaften und Weltraumforschung*, vol. 5, no. 6, pp. 335–348, 1981.

[39] J. Arbocz and H. Abramovich, “The Initial Imperfection Data Bank at the Delft University of Technology: Part I,” TU Delft, LR-290, LR-290, 1979.

[40] B. Kriegesmann, E. L. Jansen, and R. Rolfes, “Semi-analytic probabilistic analysis of axially compressed stiffened composite panels,” *Composite Structures*, vol. 94, no. 2, pp. 654–663, 2012, doi: 10.1016/j.compstruct.2011.08.033.

[41] W. Härdle and L. Simar, *Applied Multivariate Statistical Analysis*. Berlin: Springer Verlag, 2007.

[42] *Tosca*. Dassault Systèmes, 2021. [Online]. Available: www.simulia.com

[43] *Isight*. Dassault Systèmes, 2021. [Online]. Available: www.simulia.com

[44] B. Kriegesmann, “Probabilistic Design of Thin-Walled Fiber Composite Structures,” Mitteilungen des Instituts für Statik und Dynamik der Leibniz Universität Hannover 15/2012, ISSN 1862-4650, Gottfried Wilhelm Leibniz Universität Hannover, Hannover, Germany, 2012. [Online]. Available: http://edok01.tib.uni-hannover.de/edoks/e01dh12/722293151.pdf

[45] N. Gerzen, P. M. Clausen, and C. B. W. Pedersen, “Sizing optimization for industrial applications and best practice design process,” Siena, Italy, Sep. 2016, pp. 41–49. doi: 10.2495/HPSM160041.